YIELD OPTIMIZATION OF NITROGEN VACANCY CENTERS IN DIAMOND

A Thesis

by

JESON CHEN

Submitted to the Office of Graduate Studies of
Texas A&M University
in partial fulfillment of the requirements for the degree of

MASTER OF SCIENCE

August 2011

Major Subject: Physics

Yield Optimization of Nitrogen Vacancy Centers in Diamond

YIELD OPTIMIZATION OF NITROGEN VACANCY CENTERS IN DIAMOND

A Thesis

by

JESON CHEN

Submitted to the Office of Graduate Studies of
Texas A&M University
in partial fulfillment of the requirements for the degree of

MASTER OF SCIENCE

Approved by:

Co-Chairs of Committee,	Philip Hemmer
	Alexei Sokolov
Committee Member,	Alexey Belyanin
Head of Department,	Edward Fry

August 2011

Major Subject: Physics

ABSTRACT

Yield Optimization of Nitrogen Vacancy Centers in Diamond.

(August 2011)

Jeson Chen, BS, National Taiwan University

Co-Chairs of Advisory Committee: Dr. Philip Hemmer
Dr. Alexei Sokolov

Solid-state technologies for quantum mechanical application require delicate materials that can operate stably with a long coherent time. Nitrogen vacancy (NV) centers in diamond is one of the most promising materials for quantum physics, with applications such as single photon emitters, quantum computation, and magnetic sensor.

To fully exploit the capability of NV centers in diamond as magnetic sensors and quantum bits, the optimum production recipe, as well as the method to enhance its optical performance, has been studied in this work. The NV centers in bulk diamond were prepared by ion implantation and electron irradiation, and the maximized yield above certain annealing temperature and time threshold, optimum dose for magnetic sensitivity, and the enhancement of coherence time by hot irradiation are found by comparing its optical and magnetic performance both experimentally and theoretically. In addition, the enhancement of optical performance and size characterization of NV centers in nanodiamonds by means of ambient air oxidation will be discussed in this work.

With the optimum recipe to handle NV centers in diamond in this work, the current NV magnetic sensors can achieved higher sensitivity and many NV-related applications can also benefit from getting a higher yield of NV centers.

ACKNOWLEDGEMENTS

NOMENCLATURE

AFM	Atomic Force Microscopy
APD	Avalanche Photodiode
CCD	Charge Coupled Device
CVD	Chemical Vapor Deposition
DC	Direct Current
ESR	Electron Spin Resonance
FID	Free Induction Decay
HBT	Hanbury Brown and Twiss
NV	Nitrogen Vacancy Center (negatively charged)
ND	Nanodiamond
ODMR	Optical Detected Magnetic Resonance
TEM	Transmission Electron Microscopy
T1	Spin-Lattice Relaxation Time
T2	Spin-spin Relaxation Time
ZFS	Zero Field Splitting

TABLE OF CONTENTS

LIST OF FIGURES

FIGURE   Page

FIGURE   Page

LIST OF TABLES

CHAPTER I

INTRODUCTION

Detection of weak magnetic fields with high resolution revolutionizes the way of measurement in physics and medical science. A sensor able to detect magnetic fields with picotesla resolution would enable unprecedented applications, such as detection of the slight magnetic field emitted by currents within a firing neuron. Magnetic detecting techniques using superconducting quantum interference devices [1], Hall effect sensors [2] , and magnetic force resonance microscopy [3] have been studied, but these techniques required low temperature, extreme vacuum, or long data acquisition time, all of which restrict application.

On the other hand, the nitrogen vacancy centers in diamond have shown great potential as a magnetic sensor: optical spin initialization and manipulation enables non-invasive magnetic field detection at room temperature [4], and long spin coherence time facilitates ultrasensitive magnetic field detection [5]. Although NV centers have been produced and studied for 30 years [6], the recipe for high concentration production and optimum sensitivity has not yet been systematically studied. In addition, for biological applications a high concentration of NV centers is needed to have at least one NV in small nanometer sized diamond (ND) [7][8].

_____

This thesis follows the style of *Physical Review Letters*.

Here, we demonstrate both theoretical and experimental studies of the creation of high concentration of NV centers and examine their optical and magnetic properties with various doses and temperatures, and obtain an optimum recipe for bulk diamond. Moreover, the size shrinking and fluorescence enhancement methods are also explored for NDs for eventual biological applications.

CHAPTER II

THEORY

A. Diamond properties

A diamond is a transparent crystal consisting of carbon that exhibits extremely

high hardness. Table. I summarizes the properties of diamond:

Table. I Common properties of diamond

Mohs hardness	10
Molar mass	12.01 g/mol
Chemical formula	C
Crystal structure	Octahedral
Density	3.52 g/cm³
Refractive index	2.418
Thermal conductivity	900-2320 w/m · K
Optical transmission	225 nm to IR
Debye Temperature	2200 K
Displacement energy	43 to 46 eV
Binding energy	7.3 eV

Diamond's crystal structure is one of the closest packing lattice : face-centered cubic

with sp3 covalent bond, which make diamond hard and chemically inert. Using strong

acid to clean diamond is feasible and allows removal of most dirt, some amorphous

carbon, and graphite on surface without eroding the diamond.

The bond strength of diamond also allows heating in vacuum to high temperature up

to 1700°C and can be baked in air up to 700°C before converting to graphite. The

surface of bulk diamond and nanodiamond (ND) can be covered with graphite,

amorphous carbon, functional chemical groups such as C=O, O-H, and C-H. To remove

the surface layers of graphite and amorphous carbon, diamonds are either oxidized with acid such as boiling piranha solution (H_2SO_4: $H_2O_2 = 3:1$) at 500°C for 2 hours, oxidized in mixed acid solution (sulfuric acid : nitric acid : perchloric acid =1 : 1 : 1) at 90˚ C for 3.5 hours, or baked in ambient air at 400°C for a few hours. After oxidation, any C-H, $C - H_2$ or $C - H_3$ groups are completely removed, and mostly C=O and O-H groups on surface remain [9][10].

1. *Synthesized diamonds and classification*

Ordinary bulk diamond contains impurities and the color changes according to the impurity in it. In Table. II bulk diamond type is classified.

Table. II Different types of diamond

Classification				Color
Type I	Nitrogen impurity	Type IA	Clusters of nitrogen impurities.	Pale yellow or colorless
		Type IB	Single nitrogen atom impurities dispersed in diamond	Dark yellow or brown
Type II	No nitrogen impurity	Type IIA	Almost or entirely devoid of impurity	colorless
		Type IIB	Boron impurity	Light blue or grey

To produce diamond, there are a few common methods:

- High pressure high temperature synthesis (HPHT) diamonds are produced from pure carbon source at temperature around 1500°C under 5 GPa

pressure. The diamonds produced in this method contains nitrogen impurities and are mostly type Ib diamonds [11].

- Chemical vapor deposition (CVD) diamonds are formed with ionized methane and hydrogen gas where the growth completes with the hydrogen plasma etching. The diamonds produced in this method can be easily grown with selected impurities. CVD diamonds are the main source of ultrapure diamond (type IIa) [12].

- Detonation nanodiamonds are originated from detonation of a mixture of trinitrotoluene and hexogen. The typical diamond particle size produced in this method is around 5~8 nm [13].

2. *NV centers in diamond*

The substitutional nitrogen impurity with a carbon vacancy nearby in diamond is called nitrogen-vacancy center as shown in Fig. 2-1. Nitrogen vacancy center, belonging to C_{3V} pyramidal symmetric group, can be found in both natural and synthesized diamond, and the two charge states: $N-V^0$ and $N-V^-$ has optical zero phonon line centered at 575 nm and 637 nm, respectively [14].

There are 5 valence electrons covalently bonded between the nitrogen and the nearby carbon atoms, and there are 2 quasi-covalent boned electrons between the nitrogen and the vacancy site. In addition, there are one or two unpaired electrons around the vacancy and these nitrogen vacancy centers are denoted by $N-V^0$ and $N-V^-$ respectively. In this work, only negatively charged nitrogen vacancy centers will be discussed and simply abbreviated as NV.
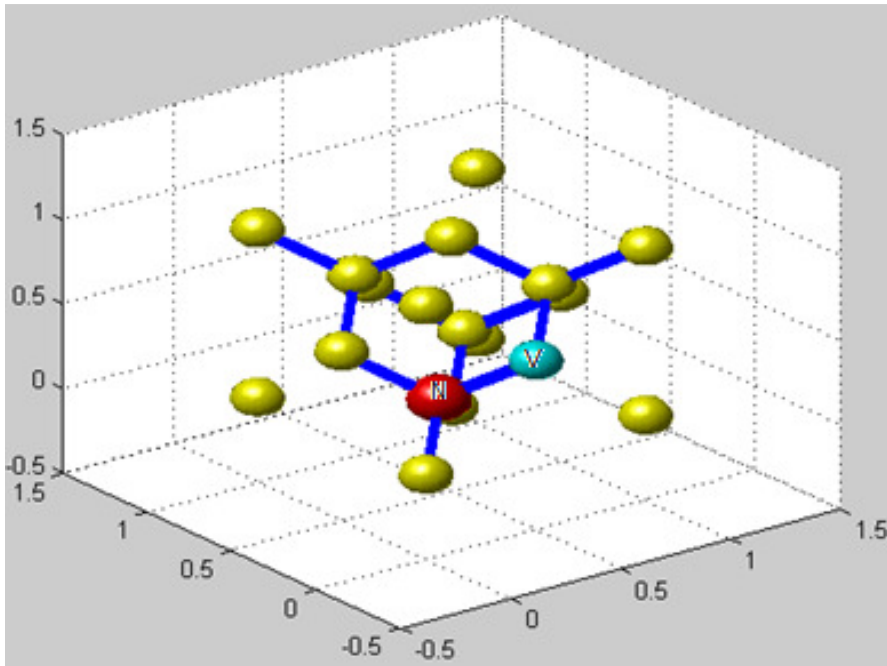
Fig. 2-1 Schematic of nitrogen-vacancy center in diamond.

The two unpaired electrons in NV center forms a spin ground triplet (S=1). The electron orbital transition between the triplet excited state ^{3}E and the triplet ground state ^{3}A are separated by 1.945eV (637 nm) with an excited state life time of 13 ns [15], while at least one metastable singlet state ^{1}A or ^{1}E in between has a life time of approximately 150-300 ns. The energy spectrum is shown as Fig. 2-2.

There are two decay channels from the excited state ^{3}E: the spin preserved channel from ^{3}E directly dropping to ^{3}A , and the indirect spin-selective channel from ^{3}E via singlet metastable state ^{1}A to ^{3}A that $m_s = \pm 1$ degenerate sublevels decaying to $m_s = 0$ is mostly favored. Thus, the net effect after a few optical pumping cycles with the two decaying channels will lead to spin polarization to $m_s = 0$ state.
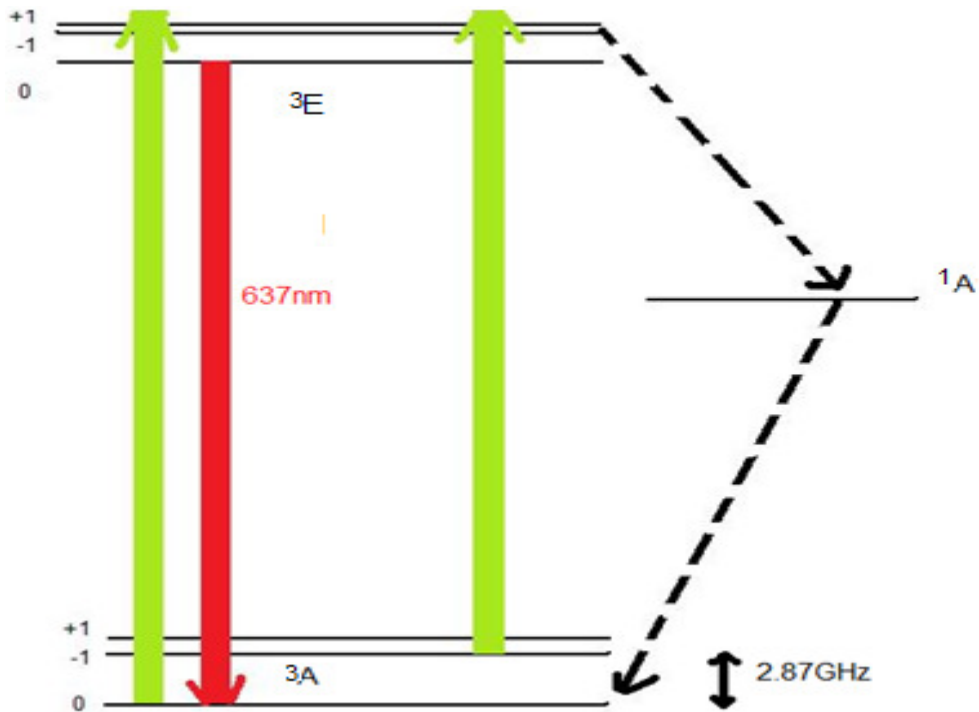
Fig. 2-2 Electron energy diagram of NV.

The electron spin Hamiltonian of NV^- is given by:

$$H_{spin} = D(S_z^2 - \frac{1}{3}[S(S+1)]) + E(S_x^2 - S_y^2) + \gamma B \cdot S)$$ (2.1)

with D the zero field splitting (ZFS) of 2.87 GHz, E the strain, γ the electron gyromagnetic ratio, and B the external magnetic field. Since there is a ZFS, the energy of $m_s = \pm 1$ states are intrinsically higher than $m_s = 0$ state without the presence of magnetic field. There is also hyperfine coupling between electron and the nearby nuclei with nonzero spin such as $^{14}_7N$, $^{15}_7N$, and $^{13}_6C$ leading to sublevels with less than 4% of zero field splitting [16].

B. Electron spin resonance

The Hamiltonian due to spin in the presence of a magnetic field aligned along the defect axis is given by

$$H = -\frac{g\mu_B}{h}\vec{S} \cdot \vec{B} \qquad (2.2)$$

where g is the gyromagnetic ratio of electron = 2.002319, μ_B the vacuum permeability, S the spin, and B is the external magnetic field.

Applying the approximation that only the component of magnetic field parallel to the NV- symmetry axis shifts the energy and the ground electron state of NV- is spin 1, a perpendicular oscillating magnetic field can make a transition from $m_s = 0$ to either of the $m_s = \pm 1$ states depending on which transition the perpendicular field is in resonance with. For small (smaller than the splitting magnetic field of [3]A of 1027 Gauss) or no axial magnetic field the m_s=0 and m_s=-1 transitions can be treated as an independent two-level quantum system:

$$\psi(t) = C_0(t)e^{-i\omega_0 t}\,|0\rangle + C_1(t)e^{-i\omega_1 t}\,|1\rangle \qquad (2.3)$$

in time-dependent perturbation theory

$$\dot{C}_i(t) = -\frac{i}{h}\sum_n \langle i|H|n\rangle\, e^{i(\omega_i - \omega_n)t}\, C_n(t)\,. \qquad (2.4)$$

Thus, the probability is given by

$$P_{0\to-1}(t) = C_1(t)^2 = [\frac{R_0}{R}\sin\left(\frac{1}{2}Rt\right)]^2 \quad, \qquad (2.5)$$

where $R_0 = \frac{g\mu_B B_1}{\hbar}$, B1 is the amplitude of the oscillating magnetic field, and

$R = \sqrt{R_0{}^2 + \delta^2}$ is the generalized Rabi flopping frequency with given frequency

detuning δ [17]. The Rabi flopping diagram is shown as Fig. 2-3.
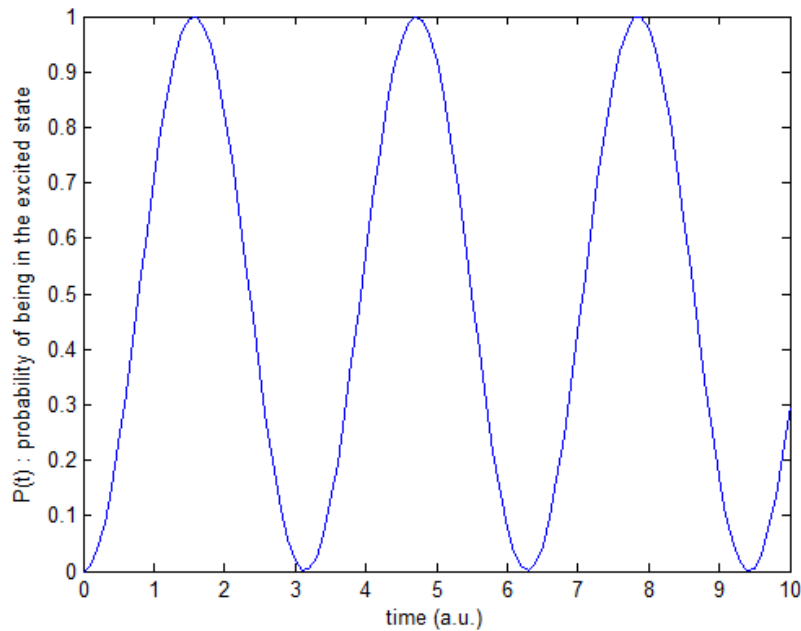
Fig. 2-3 Example of Rabi flopping of two level quantum system.

1. *Pulsed electron spin resonance*

   After finding out the Rabi frequency, the spin state may be "rotated" by different

phase angle in the Block sphere by applying microwave for some chosen time. The

simplest pulsed ESR experiment is the free induction decay. After initializing the spins

of the system to $|0\rangle$ state, the microwave pulse called $\pi/2$ pulse is applied within 1/2 of

the time duration to rotate the spin to $|1\rangle$ state as shown in Fig. 2-4.
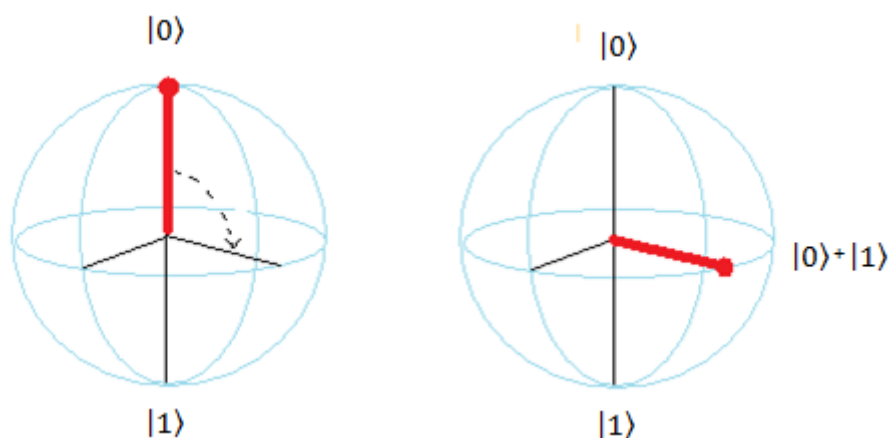
Fig. 2-4 Spin phase rotation of π/2 in Bloch sphere.

The spin ensemble system is left to develop for an adjustable time τ, after that, the signal of the spin states can be read out with the result similar to the theoretic Rabi flopping. The purpose is to measure spin dephasing during the interval τ since any such dephasing will prevent the system from returning to its original state.

Although the FID method is simple, the detected signal decays quite fast resulting from inhomogeneous broadening due to slow changes in magnetic field and spin-spin relaxation. An alternative way to monitor the spin interaction for a longer time is to apply a Hahn echo pulse sequence. Basically, the Hahn echo pulse add an extra π pulse to refocus the inhomogeneously broadening spins. The pulse sequences for FID and Hahn echo are shown in Fig. 2-5.
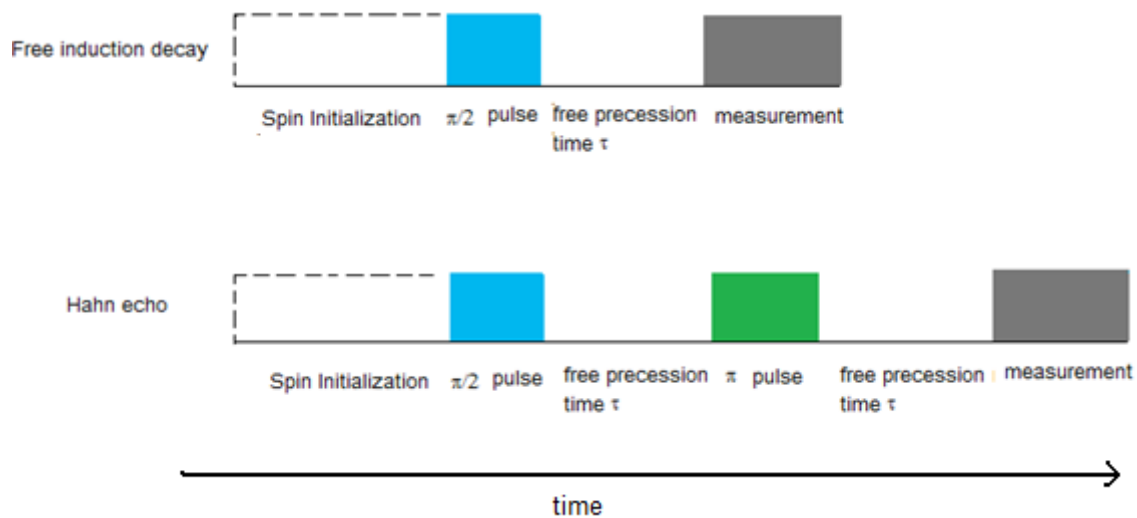
Fig. 2-5 Schematic diagram of different pulse experiments.

The spins in the system after the first π/2 pulse precess at slightly different speed and begin to spread out, but π pulse flips the precession plane and those were precessing faster now precess slower and the slower spins now precess faster. As a result, spreading spins refocus at time equal to the delay between π and π/2pulses. When the spins are precessed for the same free precession time τ, the spins are then refocused as shown in Fig. 2-6. Finally, magnetic signals that reverse sign between or change in amplitude between the first and second waiting time can be detected without inhomogeneous broadening. However, DC or slowly varying magnetic fields cannot be detected by this method.
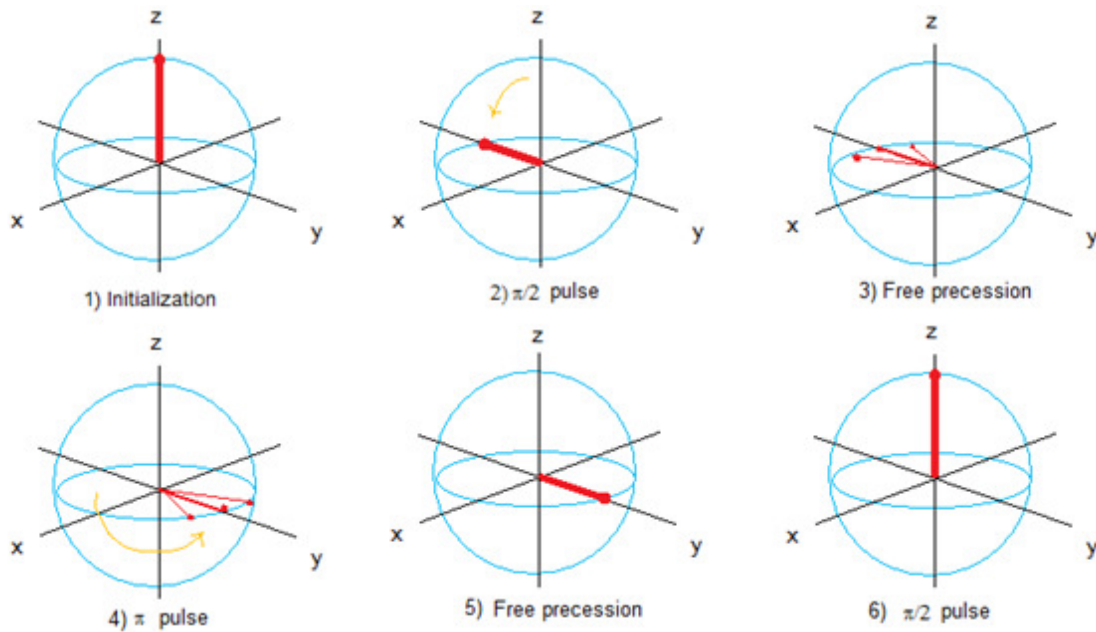
Fig. 2-6 Schematic diagram of spin during Hahn echo pulse.

2. *Spin relaxation time*

The measured signals from the spins decay exponentially with time, and there are two different intrinsic relaxation times of a spin ensemble: spin-lattice relaxation time (T1) and spin-spin relaxation time (T2). T1 characterizes the time needed for the longitudinal component of spin relative to external magnetic field to recover back to its thermal equilibrium state, whereas T2 characterizes the time for transverse component of the spin, sometimes called coherence, to decay toward zero. In general, the longitudinal spins relaxes according to

$$S_l(t) = S_{l,eq} - [S_{l,eq} - S_l(0)]e^{-\frac{t}{T_1}} , \tag{2.6}$$

and the transverse spins decay according to

$$S_t(t) = S_t(0)e^{-\frac{t}{T_2}} . \tag{2.7}$$

For NV centers in the presence of ESR defects like substitutional nitrogen centers or charged vacancies, T1 and T2 are mainly affected by these electron spins and can be shortened by implanting high concentrations. For NVs shallowly implanted near the surface additional surface spin defects can shorten T1 and T2 even more. In ultrapure crystals T1 is limited by phonons and T2 is limited by interactions with ^{13}C isotope in the lattice.

C. Photons autocorrelation function

In general, there are three different types of light sources differing by their intensity fluctuation: laser or coherent light, thermal light, and single photon emitter light as shown in Fig. 2-7. To distinguish among these, the photons autocorrelation function, or the second order coherence $g^{(2)}(\tau)$ is used, given by

$$g^{(2)}(\tau) = \frac{\langle I(t)\rangle\langle I(t+\tau)\rangle}{\langle I(t)\rangle^2},$$

(2.8)

where I(t) stands for the light intensity at time t. This can be measured experimentally and used to calculate the light source's fluctuation to determine its coherence type.
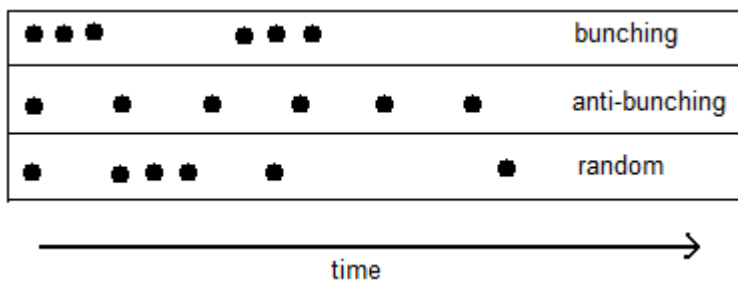
Fig. 2-7 Photons detection as a function of time and its classification.

If $g^{(2)}(\tau) > 1$, the light source is thermal light and shows "bunching" behavior.

And if $g^{(2)}(\tau) = 1$, the light source is laser-like and photons are randomly

distributed as in a Poisson distribution. If $g^{(2)}(\tau) < 1$ which arises from single

photon sources used for quantum communication and shows "anti-bunching".

$g^{(2)}(\tau)$ can be measured by Hanbury Brown and Twiss experiment that utilizes an

50% beam splitter and an turnable time delayer unit as Fig. 2-8 below.
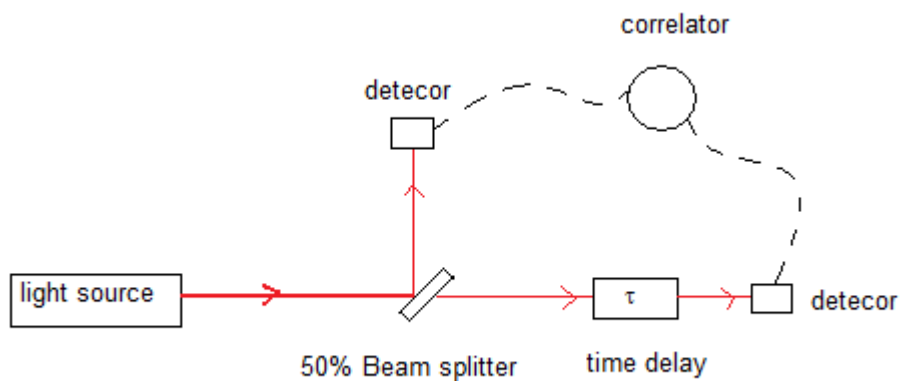
Fig. 2-8 HBT experiment setup.

CHAPTER III

COMPUTER SIMULATION

A. Ion implantation simulation

Ion implantation is the process where electric field accelerated ions are injected into materials to imbed impurities. The vacancies in diamond are the empty sites that carbon atoms were "kicked out" of by the recoil of the implanted ions. To produce the NV^- centers in type IIA diamonds, diamonds are implanted with nitrogen ions to create both nitrogen impurities and vacancies.

For the simulation of ions and vacancies' spatial distribution after ion implantation, a free academic sharing software "Stop and Range in Matter (SRIM)" made by Dr. James F. Ziegler was used as Fig. 3-1. To optimize the simulation, there are a few parameters in this Monte Carlo simulation can be chosen: the atomic number of implant ion and implanted material, the implantation energy, the implanted material density, and the implanted material displacement energy.

Those parameters for the nitrogen ion implantation experiments in diamond are: the nitrogen ion atomic number 7 and implanted carbon atomic number 6, the density of diamond 3.52 g/cm^3, and the displacement energy of carbon atom in diamond lattice 45eV [18].
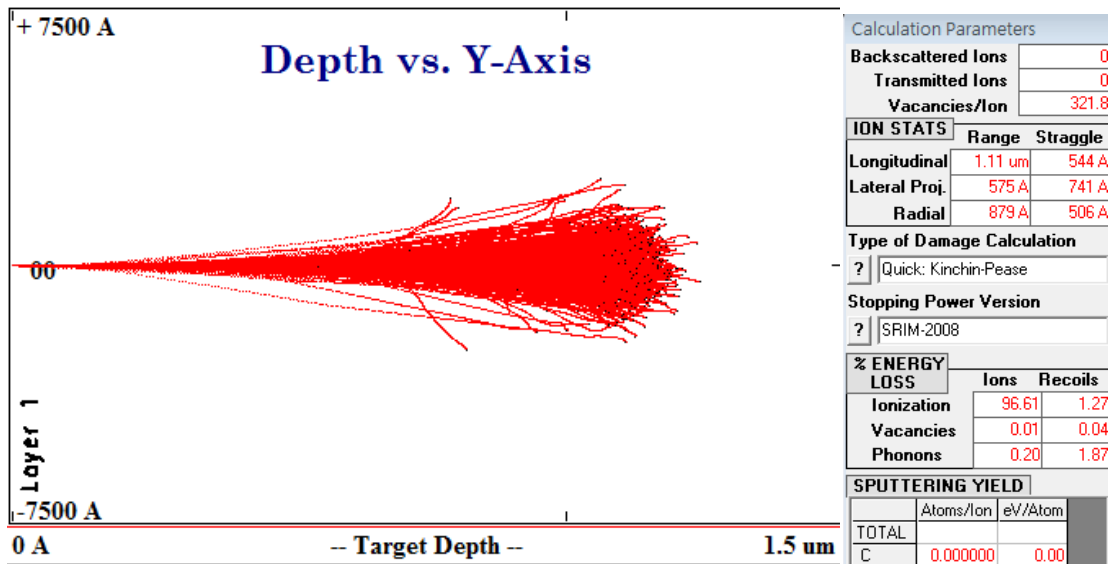
Fig. 3-1 Depth simulation of 1000 nitrogen atoms in diamond for 2 MeV implantation.

There are several important simulated results that can be readout as a parameter for further analyzing : the vacancies created per ion, the longitudinal range of ion, the straggle distance of the implanted material, the phonons energy ratio of energy loss per stopped ion. In addition, the implanted ions and vacancies concentration as a function of
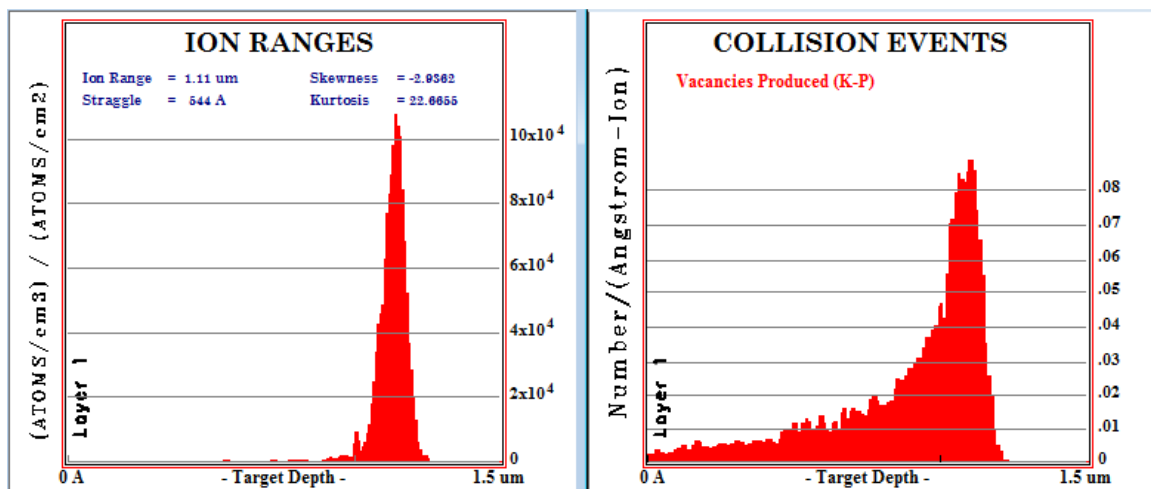
Fig. 3-2 Nitrogen and vacancies concentration simulation of 2 MeV implantation.

implanted depth can also be plotted as Fig. 3-2 and Fig. 3-3.
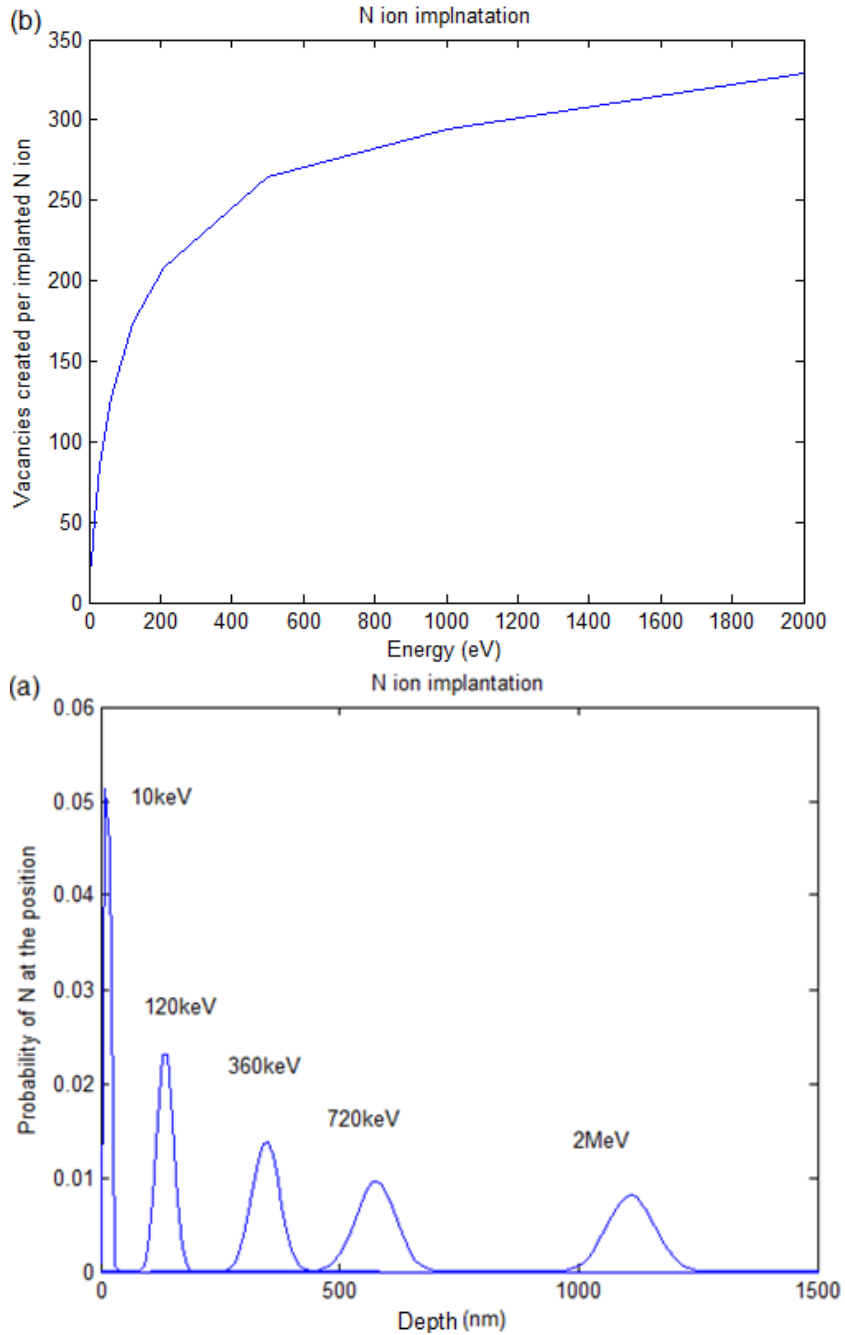
Fig. 3-3 (a) Nitrogen number as a function of depth (b) vacancy created per ion with different implantation energy based on SRIM simulation.

B. Diffusion simulation

Diffusion describe random motion of particles that cause the particles to move from regions of high concentration to regions of low concentration with a net effect that the particles slowly fill the entire mobile space as Fig. 3-4.
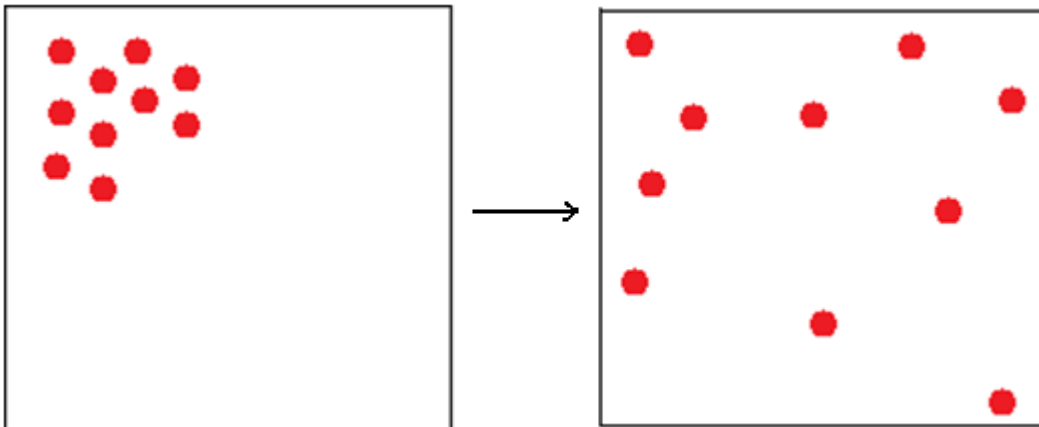
Fig. 3-4 Diffusion process.

The diffusion process can be described by Fick's Law:

1st law
$$J(r,t) = -D\nabla C(r,t) \,, \tag{3.1}$$

and 2nd law
$$\frac{\partial C(r,\ t)}{\partial t} = -\nabla \cdot J(r,\ t) \,, \tag{3.2}$$

where J is the particles flux vector, D the diffusion rate coefficient, C is the concentration of particles. Combining these two equations, we obtain Fick's equation:

$$\frac{\partial C(r,t)}{\partial t} = D\nabla^2 C(r,t) \,. \tag{3.3}$$

The vacancies and nitrogen impurities diffuse in diamond beyond certain temperature and the NV concentration will change according to different spatial distribution of

vacancies and nitrogen. The diffusion coefficient is a function of temperature given by

$$D = D_0 e^{-\frac{E_m}{k_B T}} \, ,$$

(3.4)

where D_0 is a constant depending on material, E_m is the migration barrier energy of a diffusing particle, k_B is Boltzman's constant, and T is temperature.

For simulation of the vacancies diffusion process in diamond, the leading diffusion coefficient value is reported to be 3.69×10^8 nm^2/s with the migration barrier of the vacancy between 0.42- 2.8 eV [19]. Here 1.7 eV is elected to simulate the vacancy diffusion in this work. Similarly, the diffusivity of nitrogen at different temperature can be found in Allison's report stating that there are two migration channels of nitrogen: Vacancy assisted migration energy 4.5 eV and self-diffusion migration energy 6.3 eV. [20]. Compared to vacancy, the nitrogen atoms remain static below 2200K, and the vacancy assisted nitrogen become mobile when the temperature higher than 1750K. The simulation of vacancy and nitrogen diffusion processes are shown as Fig. 3-5.

To include reasonable source term in Fick's equation to model the diffusion process during ion implantation, an additional Gaussian distributed source term is introduced and it is assumed that the implantation is cylindrically symmetric to give

$$\frac{\partial C(z,\ t)}{\partial t} = D \frac{d^2 C(z,t)}{dz^2} + \frac{\Gamma}{\sigma \sqrt{2\pi}} e^{-\frac{z^2}{2\sigma^2}} \, ,$$

(3.5)

where $\Gamma = \text{flux} = \frac{\text{number}}{\text{nm}^2 \cdot \text{sec}}$, and σ is the Gaussian standard deviation parameter.
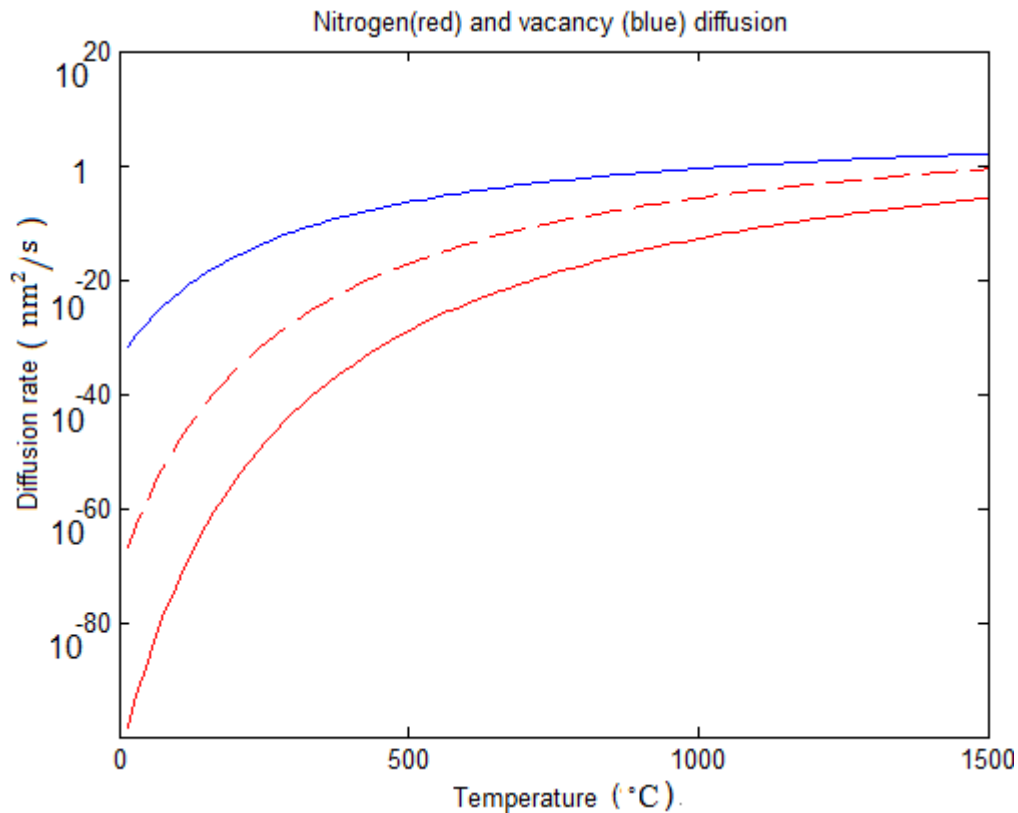
Fig. 3-5 The vacancy and nitrogen (-- for vacancy assisted nitrogen) diffusion coefficient as a function of temperature.

The modified dynamic diffusion process can be solved by applying the

following two boundary conditions:

$$C(\pm\infty, t) = 0 , \tag{3.5}$$

$$\frac{\partial C(0,\ t)}{\partial z} = 0 , \tag{3.6}$$

which sets the concentration at infinity to be zero and the concentration a local

maximum at the center. (The coordinate is chosen such that the center of the Gaussian

implanted source is located at the origin)
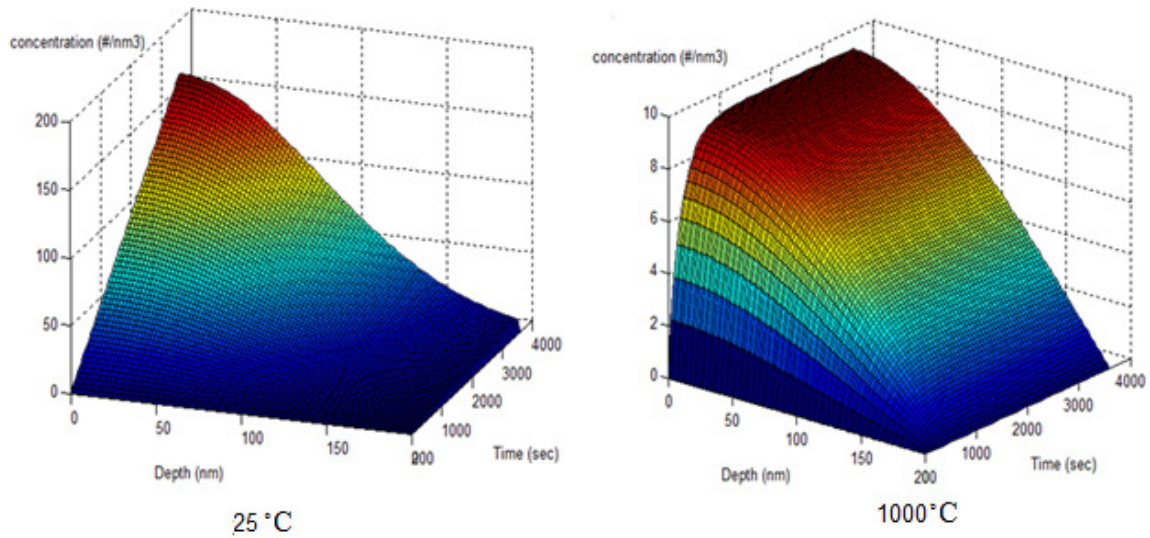
Fig. 3-6 The vacancies concentration as a function of depth and time at different temperatures during 2 MeV nitrogen implantation with total dose = 100 N/nm^2 . Note that the concentration of vacancies goes below graphitization threshold for temperature higher than 1000°C.

By Gaussian-fitting the room temperature ion implanted data from SRIM simulation as a source term in the modified Fick's equation (3.4) with software compiled in Matlab, the dynamic solution can be obtained at different temperature as Fig. 3-6.

It was reported [21] that there is a graphitization threshold for ion implantation in diamond independent of ion species and implantation energy: diamond crystal transforms into graphite when concentration of vacancies exceed 10 V/nm^3 and will not turn back to diamond after annealing.

In order to maximize the yield of NV centers, the implantation of nitrogen should be done at the maximum possible dose to produce the most nitrogen and vacancies but must always stay below the graphitization threshold. However, the implantation duration and the temperature determine the resulting local vacancies concentration and, thus, an overall consideration of parameters has to be chosen to qualify the maximum possible

yield requirement. By using the diffusion simulation in this work, the optimum

parameters can be determined to meet the requirement as Fig. 3-7.
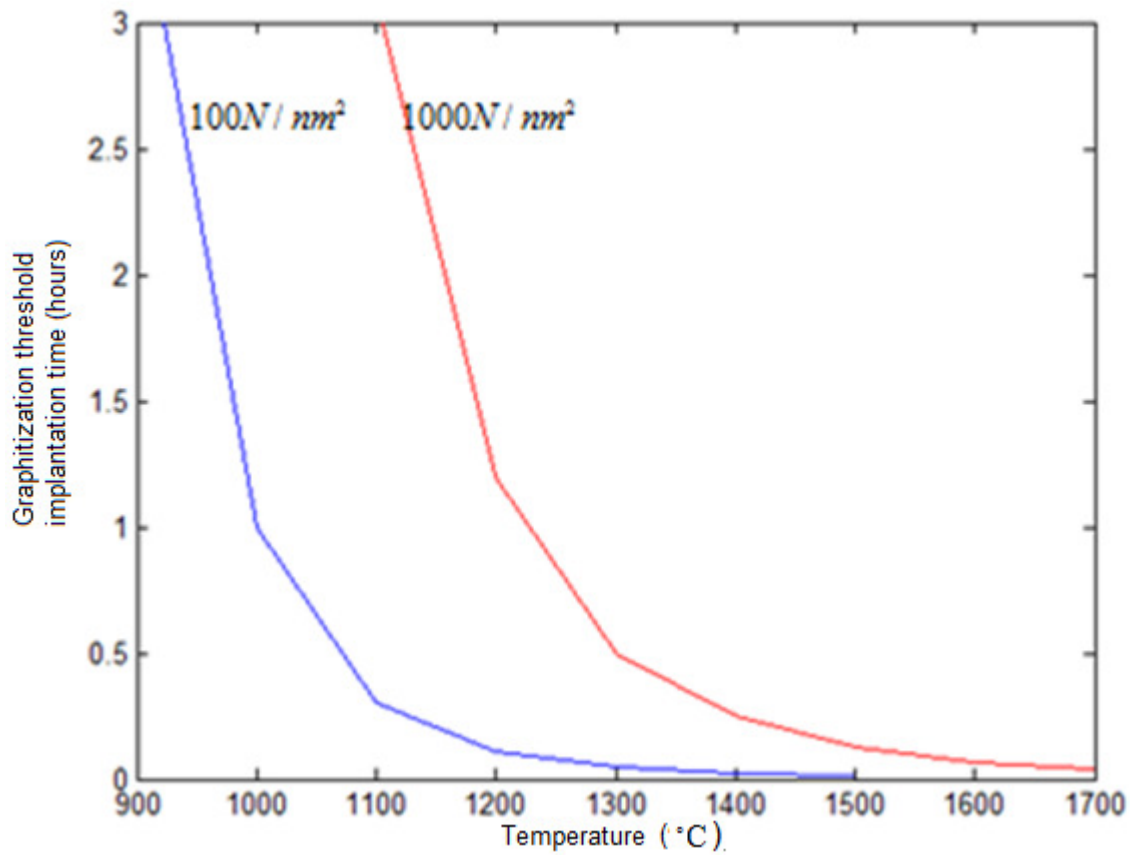
Fig. 3-7 The minimum implantation time to prevent graphitization versus temperature for various doses of 2 MeV nitrogen implantation.

C. Reaction simulation

The vacancies in 1B diamond or nitrogen implanted diamond undergo reactions:

All temperature

$$V + e^- \leftrightarrow V^-, \tag{3.7}$$

T> 600°C

$$V + N \rightarrow NV \quad , \tag{3.8}$$

$$NV + N \leftrightarrow NV^- + N^+. \tag{3.9}$$
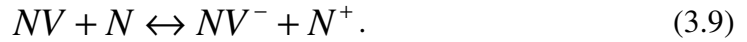
The nitrogen atoms act like electron donors in diamond and enable free electron transport. In nitrogen rich diamonds, the negative charged vacancy V^- (ND1 optical absorption band) is the dominant defect and its concentration can be an order of magnitude more than the concentration of neutral vacancy V (GR1 optical absorption band).

The nitrogen concentration for the growth of NV is dependent on the growth sector of the high pressure high temperature process [22]. In addition, the yield of NV^- is 10~40 times greater than the yield of NV^0 for 1B diamond after electron irradiation and the following annealing [23]. It is also observed that the NV yield reducing vacancy-interstitial recombination which often appears in IIA diamond doesn't occur on nitrogen rich diamond [24].

The first explanation of the creation mechanism of the NV center in 1B diamond was done by G. Davies in 1992 [25]:

$$\frac{d[V^-]}{dt} = -r_c \frac{[V^-]}{r} + r_c[V] , \tag{3.10}$$

$$\frac{d[V]}{dt} = -(r_c + r_a)[V] + r_c \frac{[V^-]}{r} , \tag{3.11}$$

$$\Delta[V] + \Delta[V^-] = \Delta[NV^-] , \tag{3.12}$$

where r_c is the reaction rate of charge conversion, r_a the decay time due to annealing, and r the equilibrium ratio of $[V^-]/[V]$. However, he calculated reaction rate by converting the optical absorption to concentration with

$$O_{GR1} = f_{GR1} [\ V \ ] \tag{3.13}$$

and fitted his experimental data. The converting coefficient he used $\frac{f_{ND1}}{f_{GR1}} = 4$ is contrary

to what is experimentally derived later : $f_{ND1} = 4.8 \times 10^{-16} \text{meV} \cdot \text{cm}^2$ [26] and

$f_{GR1} = 6 \times 10^{-17} \text{meV} \cdot \text{cm}^2$ [27]. In addition, the growth of negatively charged

divacancy V_2^- in irradiated 1B diamond above 600C reported by Joseph Kiprono [28]

can't be explained if all the vacancies form NV centers. In this work, the new dynamic

model of NV center as well as V_2^- formation will be discussed in the following.

Assume that the negatively charged divacancy V_2^- forms via the following reaction

$$V + V^- \rightarrow V_2^- \tag{3.14}$$

instead of capturing an electron from neutrally charged divacancy, because there is no

neutrally charged divacancy observed in 1B diamond [29]. The other assumption is that

the formation of NV^- involves the diffusion and reaction of neutral vacancy only, since

the charged vacancy doesn't diffuse [23].

The re-fitting of the 750°C annealing data of 1B diamond by G. Davies [6] is done as

Fig. 3-8 with the up-to-date experimental optical absorption coefficient and the

mixture of mutual charge conversion, first, and second order kinematics:

$$\frac{d[V]}{dt} = -(a \cdot r_v + r_c)[V] - (1 - a)r_v[V][V^-] + r_c\frac{[V^-]}{r}, \tag{3.15}$$

$$\frac{d[V^-]}{dt} = -r_c\frac{[V^-]}{r} - (1 - a)r_v[V][V^-] + r_c[V], \tag{3.16}$$

$$\frac{d[NV^-]}{dt} = b \cdot a \cdot r_v[V], \tag{3.17}$$

where r_c is the charge conversion rate, r_v is the first order vacancy reaction rate, r the
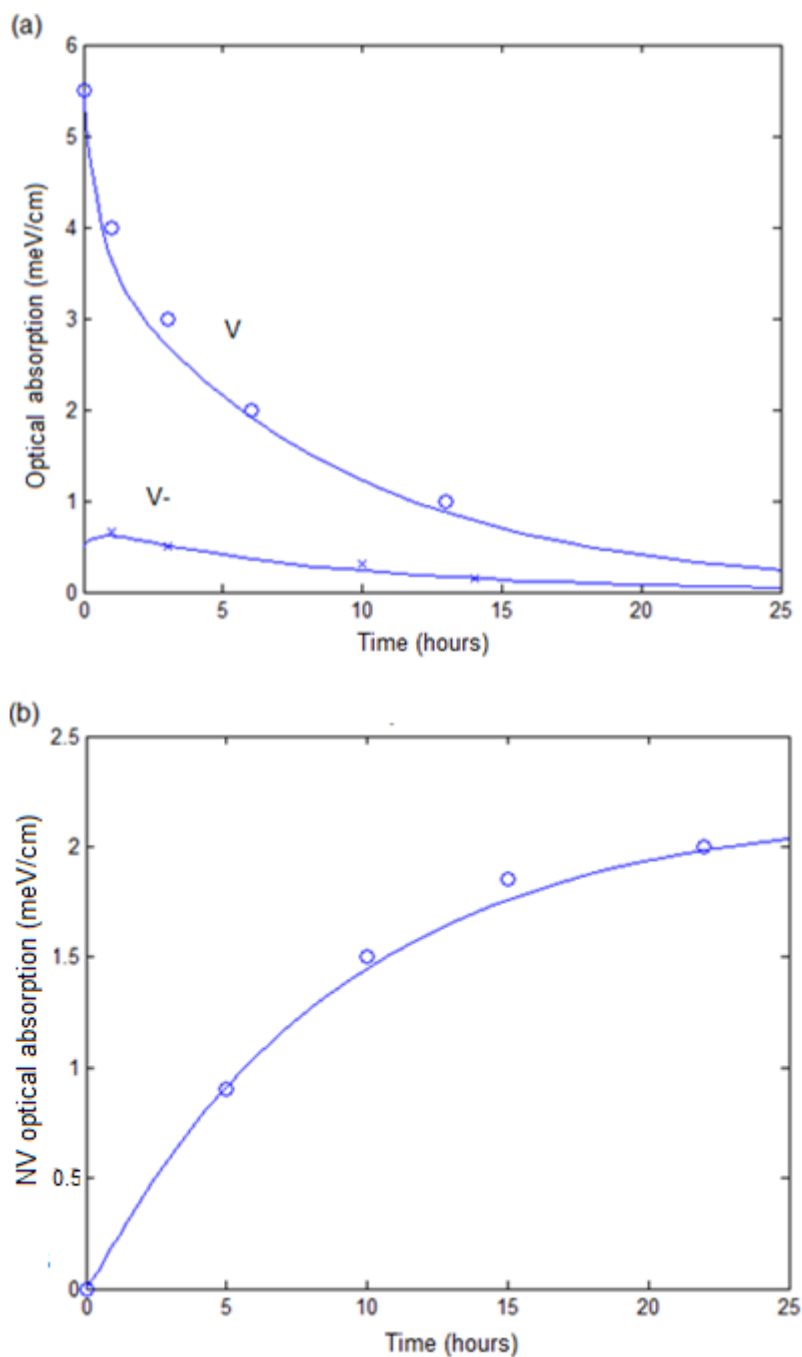
Fig. 3-8 Re-fitting of the experimental absorption data of 750°C annealing of 1B diamond irradiated to a dose of $10^{16} \sim 10^{17}$ e/cm^2 with 2 MeV electrons by G. Davies. (a) ND1 and GR1 with parameters: a=0.9, r_v= 0.2, r_c=0.7, and r =0.6 . The strength of optical absorption A is derived by integrating the absorption coefficient $\mu(E)$ (measured in cm^{-1}) at photon energy E (measured in meV) over the zero-phonon line: $A = \int \mu(E) dE$. (b) NV line with parameter b= 0.84 and $f_{nv} = 1.35 \times 10^{-16}$ meV $\cdot$ cm^2.

equilibrium ratio of $[V^-]/[V]$, a is the ratio of vacancy trapped by any sink to all the lost

vacancies, and b is the ratio of $[NV^-]$ formation to vacancy trapped by any sink.

In addition, the equation for temperature dependence of reaction rate is used

$$r_v = r_{v0} e^{-\frac{E}{k_B T}} \tag{3.18}$$

with the activation energy E of 2.3eV for vacancy capturing by sink reaction [25].

For vacancy created by electron irradiation, the conversion between electron irradiation

dose and vacancy concentration is 2 vacacnies/electron $\cdot$ cm [23]. Using these

equations and the same parameters for the simulation of 750°C annealing of 1B diamond

above, the dynamic growth of NV center for 30 minutes isochronal annealing at different

temperatures can be simulated and compared with the work by G.Davies [6] as Fig. 3-9.
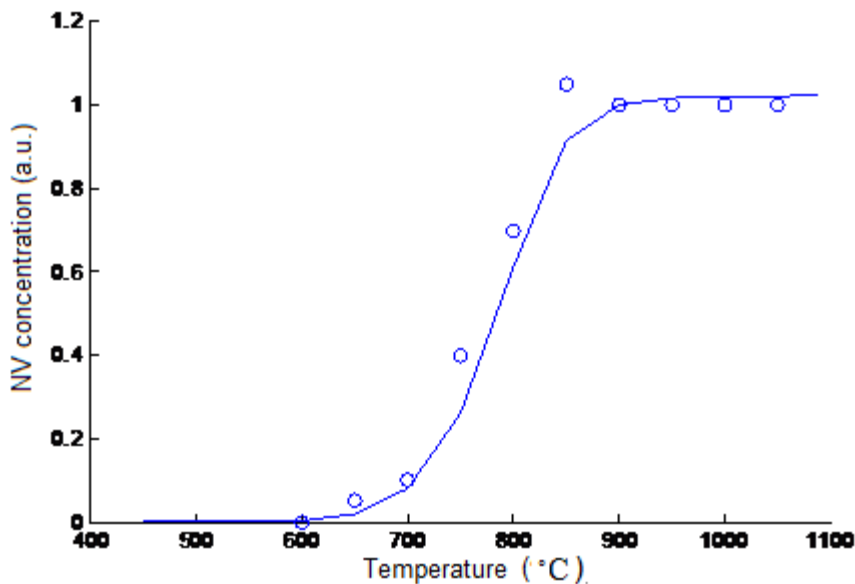
Fig. 3-9 Simulation of the NV center growth after 30 minutes isochronal annealing and comparison to the work of G. Davies in 1976 of 2 MeV electron irradiated 1B diamond with a dose of $5 \times 10^{17} e/cm^2$. The parameter used is $r_{v0} = 1.25 \times 10^7$, and it is assumed that 70% of the initially created vacancies are V^-.

Given initial implantation or irradiation dose, the annealing temperature and time to yield the maximum NV yield can be calculated by the same simulation as Fig. 3-10.
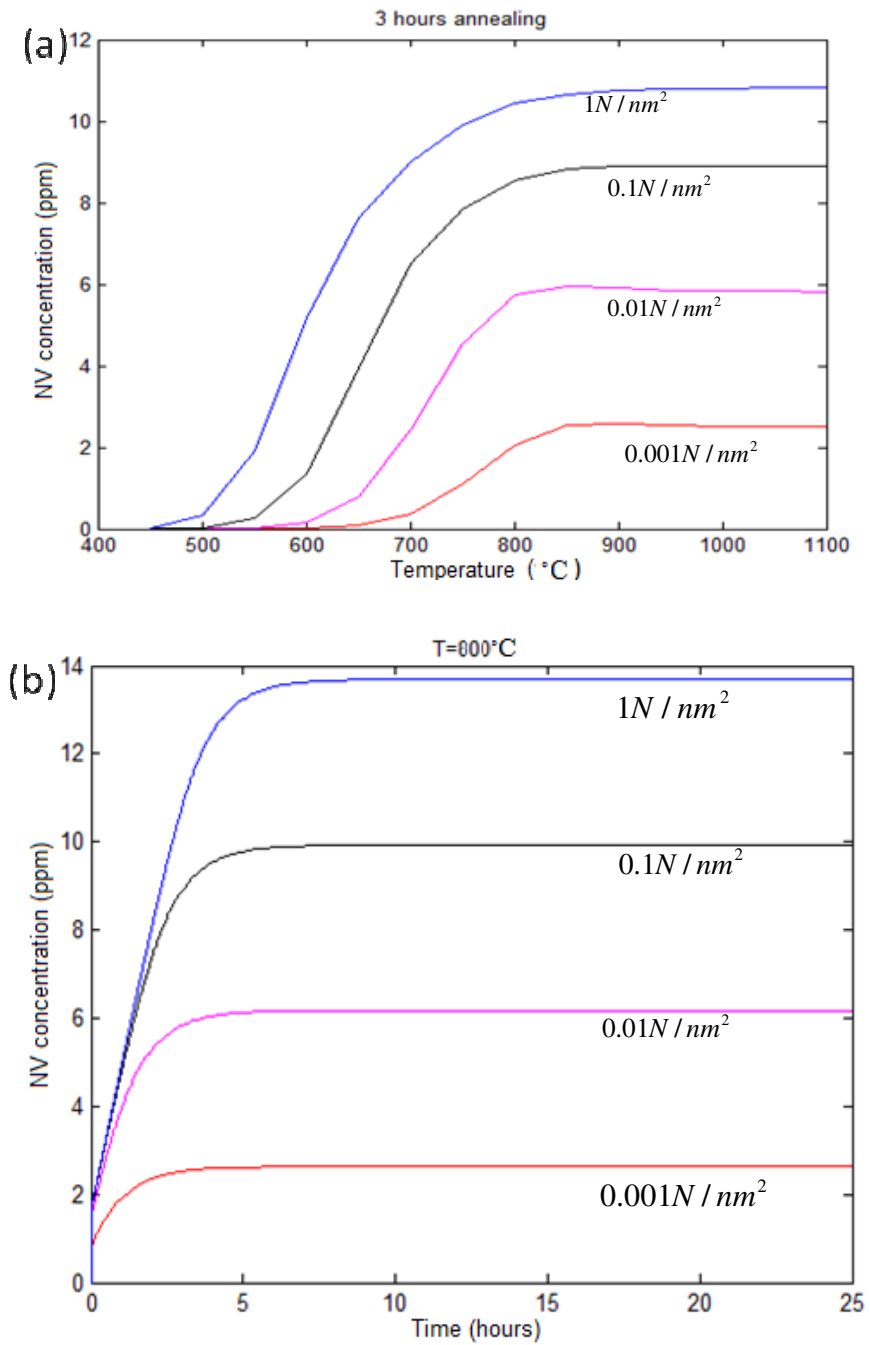
Fig. 3-10 NV concentration with different nitrogen implantation doses as a function of (a) annealing temperature (b) annealing time at 800°C.

CHAPTER IV

EXPERIMENT

A. NVs optimization in bulk diamond

To create a substitutional nitrogen impurity with an adjacent carbon vacancy (NV) in diamond, there are two different ways:

(1) Ion Implantation

To produce the NV^- centers in type IIA pure diamonds, diamonds are implanted with nitrogen ions to create both nitrogen impurities and vacancies. In this work, a 2 MeV ion implantor has been used to create a large amount of vacancies per injected nitrogen ion in a commercial Element 6 electronic grade type IIA 3 mm x 3 mm diamond.

(2) Electron Irradiation

For type IB diamond, the intrinsic nitrogen contents is around 75 ~200 ppm, and thus only additional vacancies are required in these kind of diamond to create NV centers. In this work, a transmission electron microscope (TEM) JEOL-2010 has been used to create vacancies on type IB diamond with an energy of 200 keV.

1. Ion implantation

Ion implanter consists of an ion source, accelerator, and a target chamber. The ion source emits ions proportional to the excitation current applied. After ionization, the ions are accelerated and pass through mass/charge selector to be filtered out the desired charged ion. Then, the selected ions are accelerated by high DC voltage and pass through series of focusing magnets until impinging onto the sample mounted in the

target chamber as Fig. 4-1.
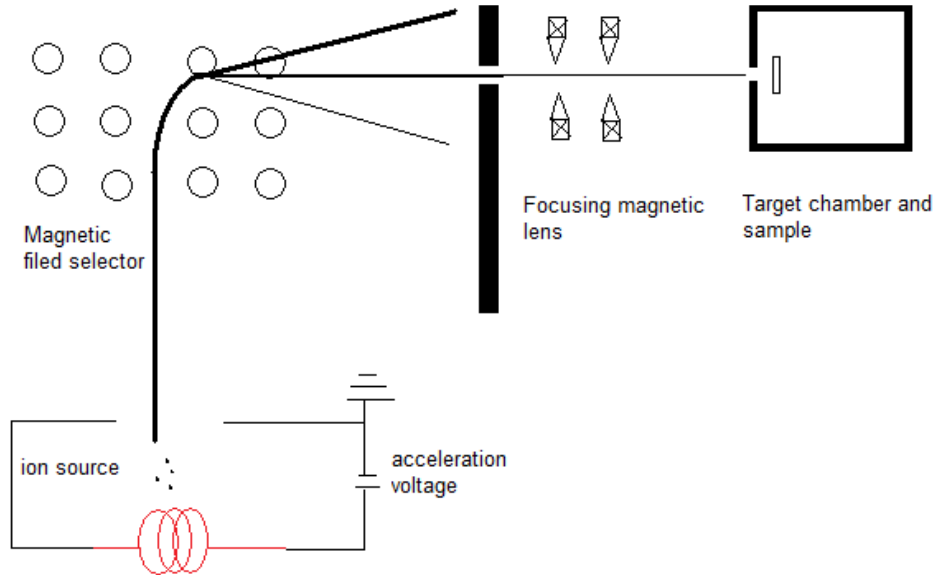
Fig. 4-1 Ion implanter.

   The ion implanter used in this work is Dynamitron electron beam particle accelerator (IBA Industrial, formerly Radiation Dynamics) capable of implantation energy from 300keV to 50MeV at Ruhr University at Bochum. Before ion implantation, diamonds are ultrasonicated in acetone solution for 30 minutes. Then 10 MeV $^{14}_{7}N^{-}$ ions are implanted into diamonds with flux $3.2 \times$ ions/s $\cdot$ cm^2 .

2. *TEM irradiation*

   Transmission electron microscope (TEM) is a microscope using electrons and electromagnetic lens instead of photons and optical lens. Since the Rayleign resolution for lens is given by

$$\Delta l_r = \frac{1.22\lambda}{D} \, , \qquad (4.1)$$

with the Angstrom scale de Broglie wavelength of the electron enables nanometer
resolution.

The basic components of TEM consist of a filament (electron gun), magnetic lens,
apertures, a vacuum chamber, and a charge coupled device (CCD) camera as Fig. 4-2. In
this work, high energy electrons from the TEM are used as a vacancy creation source for
NV center creation.
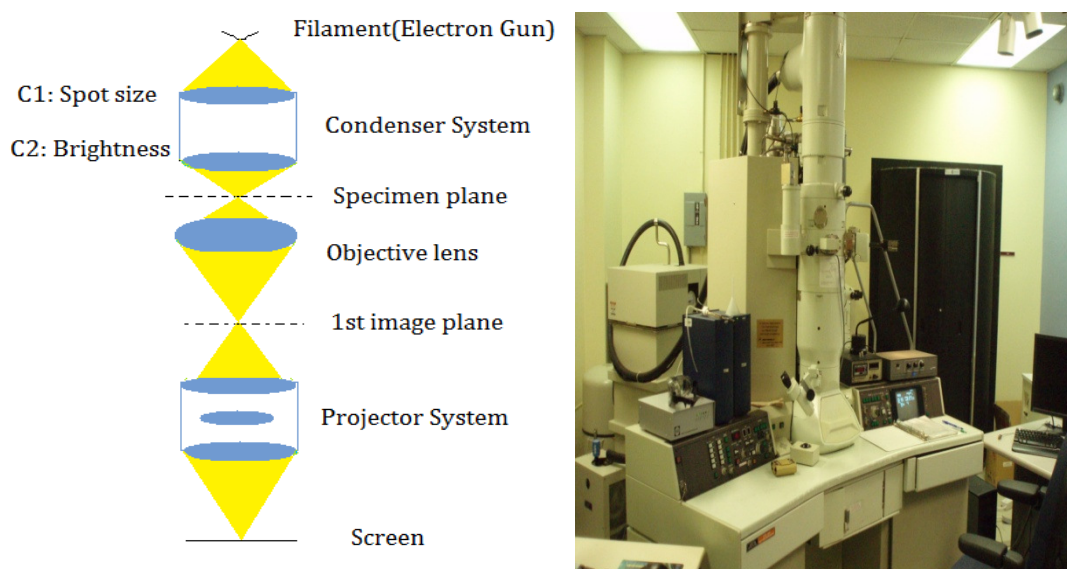
Fig. 4-2 TEM components and TEM (JEOL JEM-2010).

The TEM used in this work is JEOL JEM-2010 with LaB6 filament. Diamond
samples with thickness less than 0.5 mm are cleaved to fit in the 3mm TEM sample
holder, and then are clamped between two Molybdenum grids (SPI 4260M-MB) and
mounted on a single-tilt heating holder (Gatan model 628). The stage can reach
temperatures up to 1000°C The beam current density for irradiation is between 75~120

pA/cm^2 with 200 keV voltage, and the beam spot size on the TEM phosphor screen is 1~2 cm in diameter with magnification set to be 100 kx for highest flux. Since the actual magnification is about 75% of that on the screen, the magnification is around 75 kx.

Then the total electron dose is calculated by

$$\text{dose} = J \times t \times \left. A_{screen} \middle/ M_{film}^2 \right. ,$$ (4.2)

where J is the current density, t the irradiation time, A_{screen} the spot area on the screen, and M_{film} the actual magnification on film.

3. *Cleaning and annealing*

After ion implantation/ electron irradiation experiments, the diamonds are boiled with mixed acid solution (sulfuric acid : nitric acid : perchloric acid =1 : 1 : 1) at 90°C for 3.5 hours in a condenser system to remove surface graphite, some of the amorphous carbon atoms, and other contamination. In order to diffuse the vacancies and form NV centers, the acid cleaned diamonds are then heated up in vacuum chamber at around 800C in 10^{-6} torr for 3 hours (the heating rate is 20°C /min). Finally, the diamonds are ultrasonicated in acetone for 10 minutes to remove surface residues.

4. *ODMR measurement*

To characterize the NV center in diamond, a home-built optical detected magnetic resonance (ODMR) setup as shown in Fig. 4-3 has been used to measure NV center concentration, ESR line shape, and Rabi oscillation by fluorescence intensity.
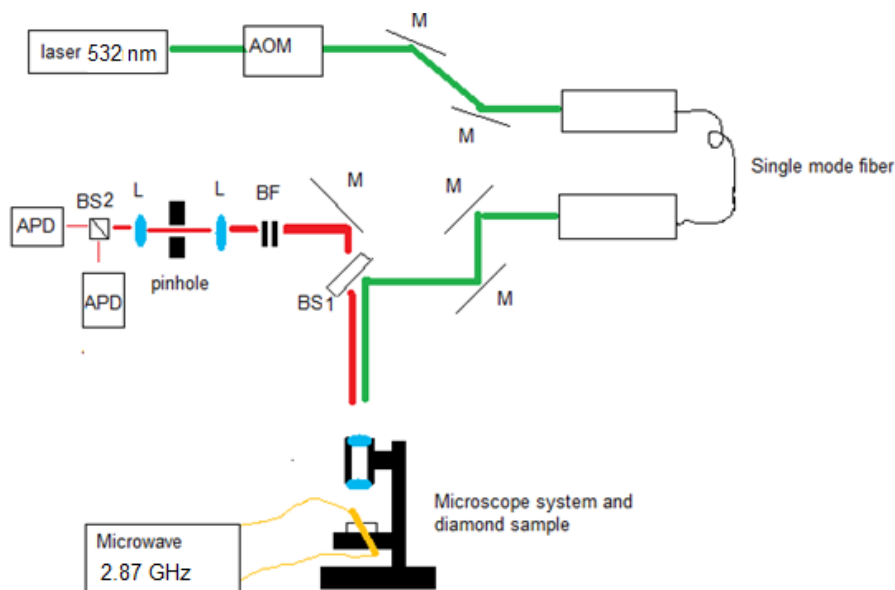
Fig. 4-3 ODMR experimental setup. AOM is the acoustic optical modulator, M are the mirrors, BS1 is a 5% reflectance beam splitter, BF is a 530 nm bandpass filter, L are the convex lenses with focal length 15cm , BS2 is a 50%-50% beam splitter, and APD is the avalanche photodiode.

The linear relationship between photon counts rate and laser power is shown as Fig. 4-4. The fluorescence photon count rate subtracted with the background counts at each pixel is in proportion to the local NV concentration and the laser power, and the NV center numbers might be estimated by dividing it with the single NV center photon count rate. The pixel size for the measurement in this experiment is around $0.25 \ \mu m^2$ and the single NV photon counts is 70k counts/2μs with 2.36mw 532nm excitation laser.
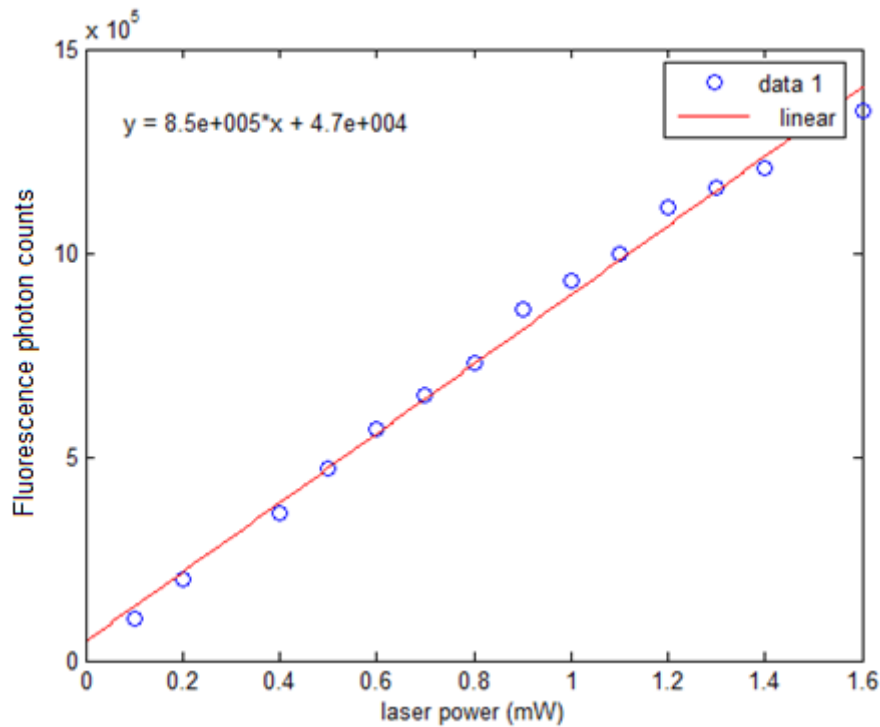
Fig. 4-4 Fluorescence photons counts versus 532 nm excitation laser power for dose 0.1 N/nm^2 of sample 12C. The estimated number of NV centers per pixel is around 29.

The photon count rate are measured at different nitrogen dose implanted spots as displayed in Fig. 4-5 with normalized laser intensity of 20μW. The fact that vacancy concentration reaches graphitization threshold when nitrogen implantation dose is larger than 10^{15} $N/_{cm^2}$ explains the decrease of fluorescence intensity beyond 10^{15} $N/_{cm^2}$ dose.
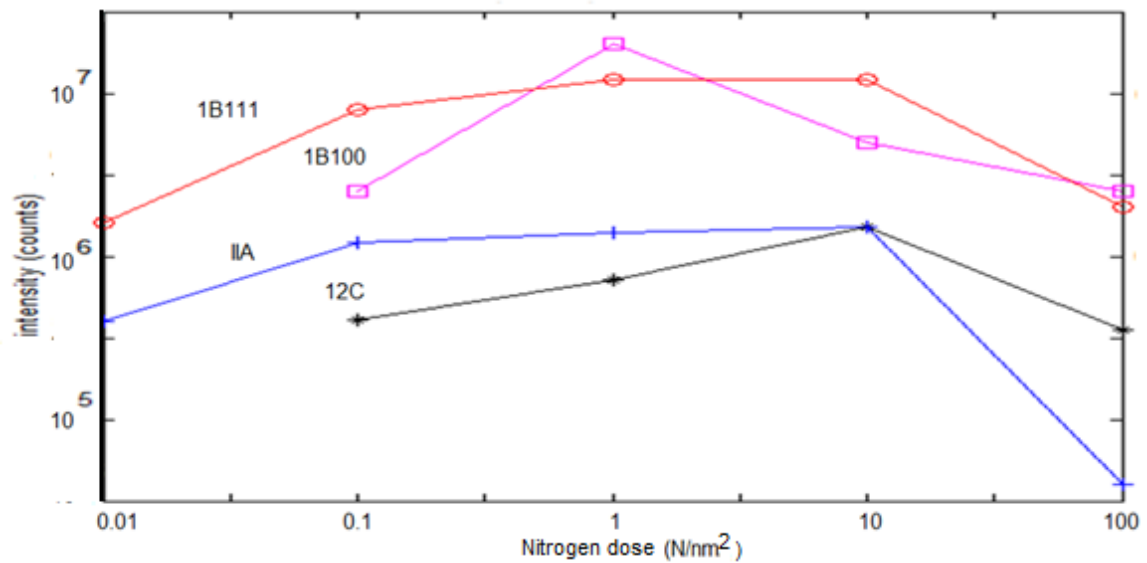
Fig. 4-5 The fluorescence intensity versus different doses of 10MeV nitrogen implanted diamonds: IIA is a pure diamond with natural abundance of ^{13}C isotope (1.1%). 12C is a diamond with less than 0.1% ^{13}C isotope. 1B100 and 1B111 are nitrogen-rich type IB diamonds with different growth sector along 100 and 111 crystal directions.

To measure ODMR, the pulse sequence below has been applied for Rabi measurement. The additional laser pulses used for spin initialization and optical readout have been added to the free induction decay and Hahn echo pulse sequences and are synchronized with the microwave pulse by Data timing generator (Tektronix DTG 5274). A schematic diagram for the ODMR pulse sequence is shown in Fig. 4-6 below, and the measured ODMR results are shown in Fig. 4-7.
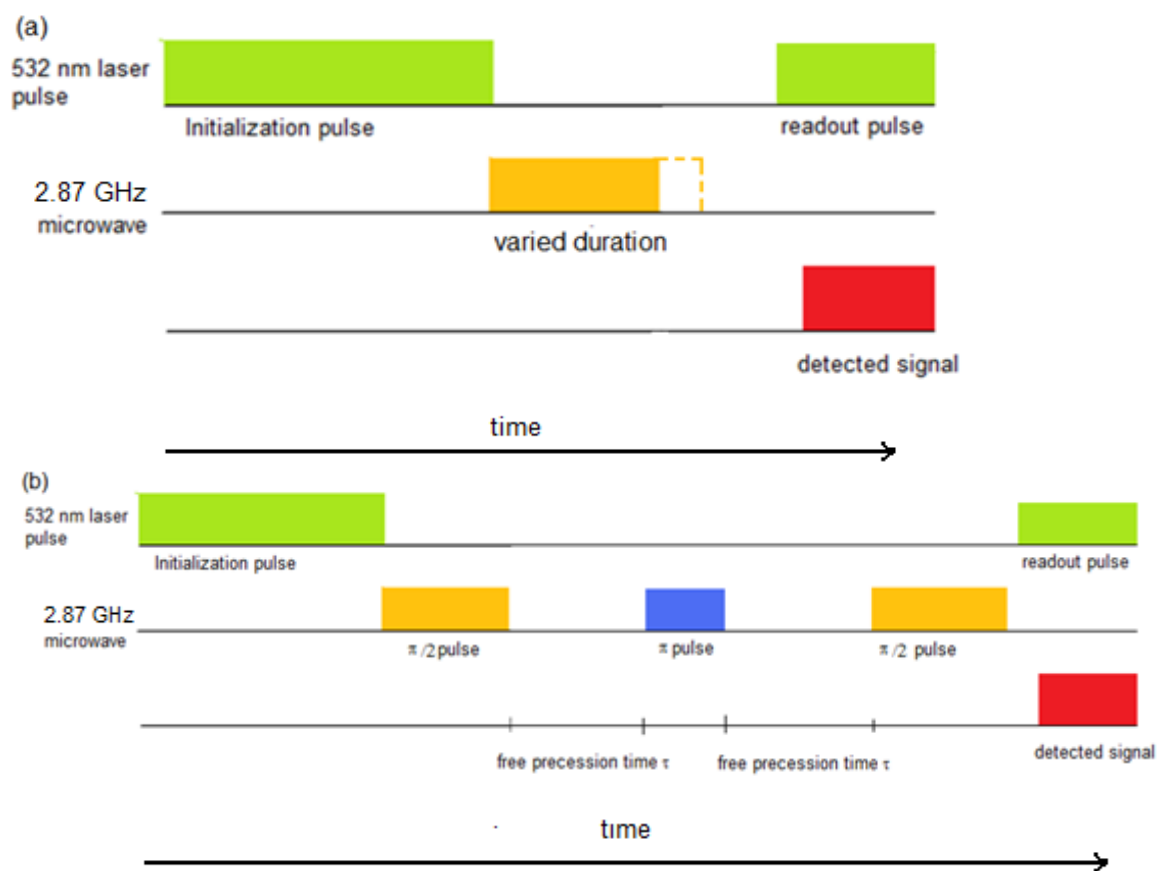
Fig. 4-6 Pulse sequence of ODMR of (a) Rabi oscillation (b) Hahn echo.
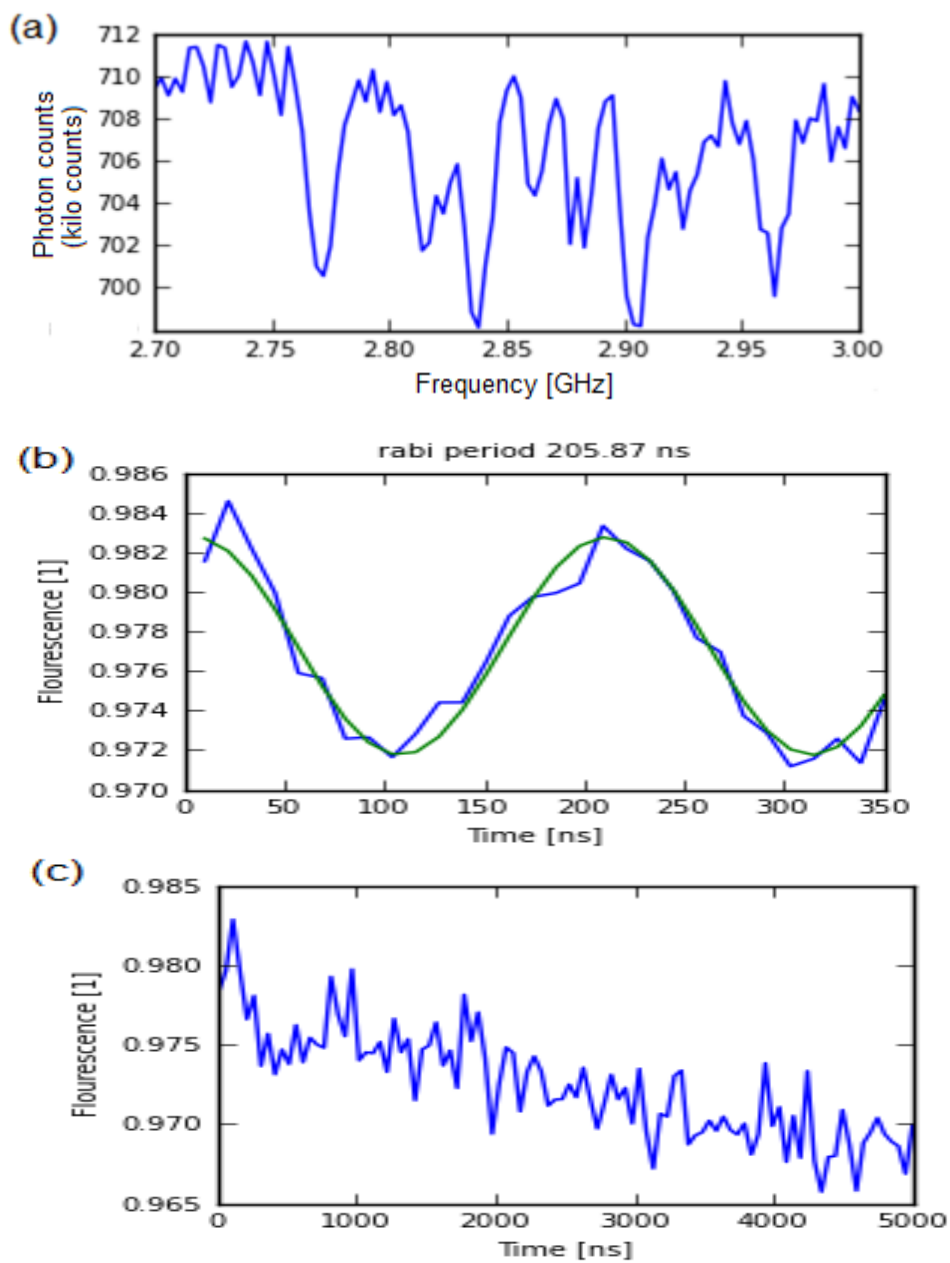
Fig. 4-7 ODMR of single NV center (a) ESR line shape (b) Rabi oscillation with normalized fluorescence (c) Hahn echo measurement with normalized fluorescence. (exponential fitted value of T2 is around 17μs).
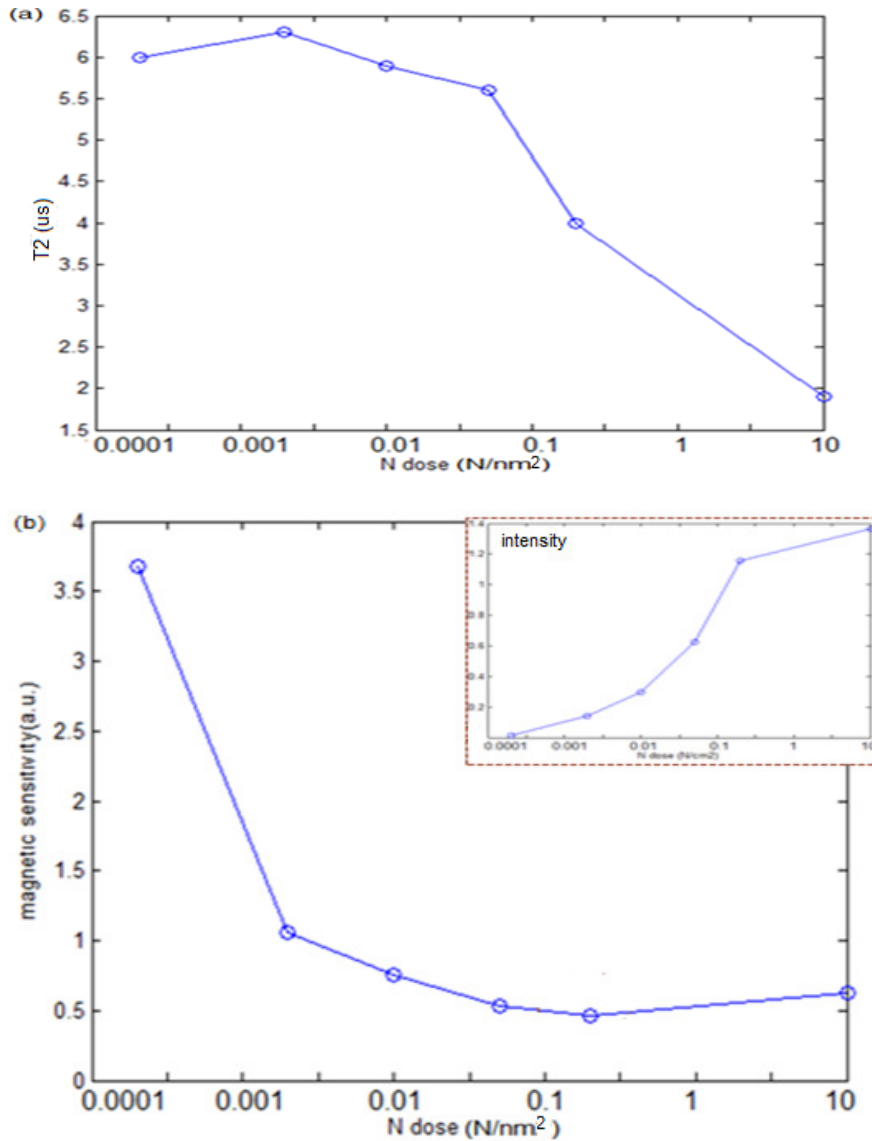
Fig. 4-8 (a) T2 measurement of HP sample implanted with 7.5 keV nitrogen ions. In addition, the calculated magnetic sensitivity is shown as (b). Intensity is shown as inset.

Another 7.5keV nitrogen implanted diamond sample measured in HP lab is shown as Fig 4-8. The minimum detectable magnetic field can be approximated [23] by

$$\delta B \approx \frac{1}{\sqrt{C_{NV^-} \cdot T_2}} \ , \tag{4.3}$$

where C_{NV^-} is the concentration of NV centers. By substituting the concentration of NV

centers with measured photon counts, the optimum dose for best magnetic sensitivity can be determined to be around 0.4 N/nm^2.

5. *Hot irradiation*

It can be inferred from Baker's work [30] that most of the non-zero spin vacancy centers (mainly V2 and V3) transformed into V11 complex above 1000C and the effective numbers of non-zero spin vacancy center decrease. Thus, high temperature electron irradiated type IB diamond has been studied in this work to enhance the magnetic sensitivity of NV centers. The IB diamond sample studied in this work was first irradiated at 210°C and then irradiated at 968°C. The measured Rabi oscillation is displayed in Fig 4-9.

Due to low signal to noise ratio of measurement in 1B diamonds, T2 can't be measured and Rabi decaying time is measured instead. The detected signal can be fitted with

$$S_{ig} \propto e^{-\frac{t}{t_R}} \sin(Rt + \phi), \tag{4.4}$$

where t_r is the Rabi decaying time, R the Rabi frequency, and ϕ is the phase angle.

Fig. 4-9 Rabi oscillation of electron irradiated IB diamond with fluorescence normalized to one. The electron doses are both 10^{22} e/cm^2 for both curves.

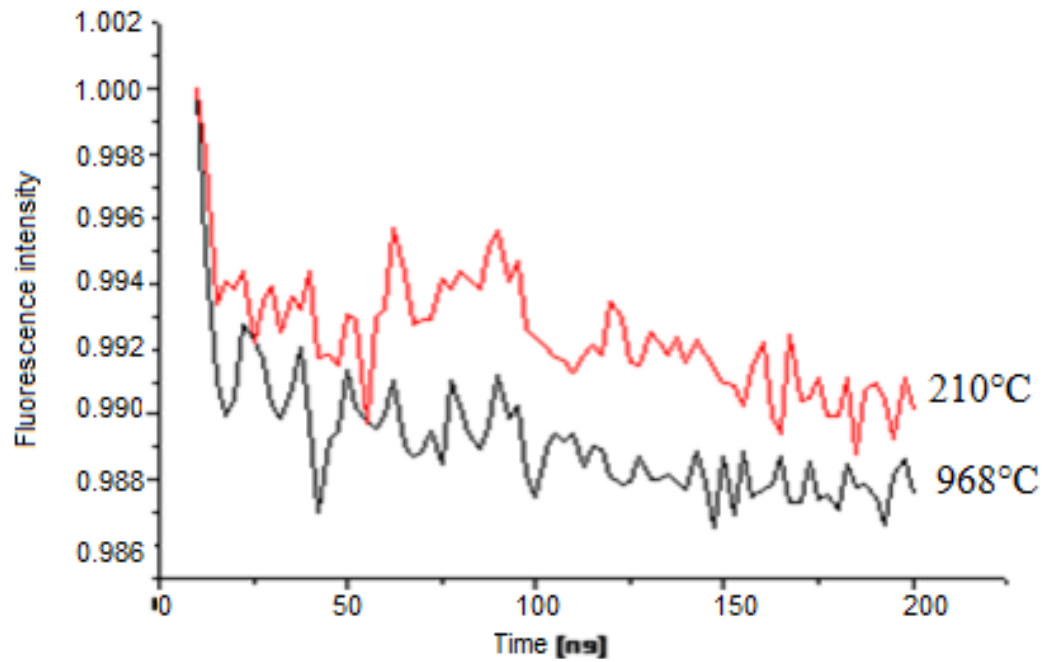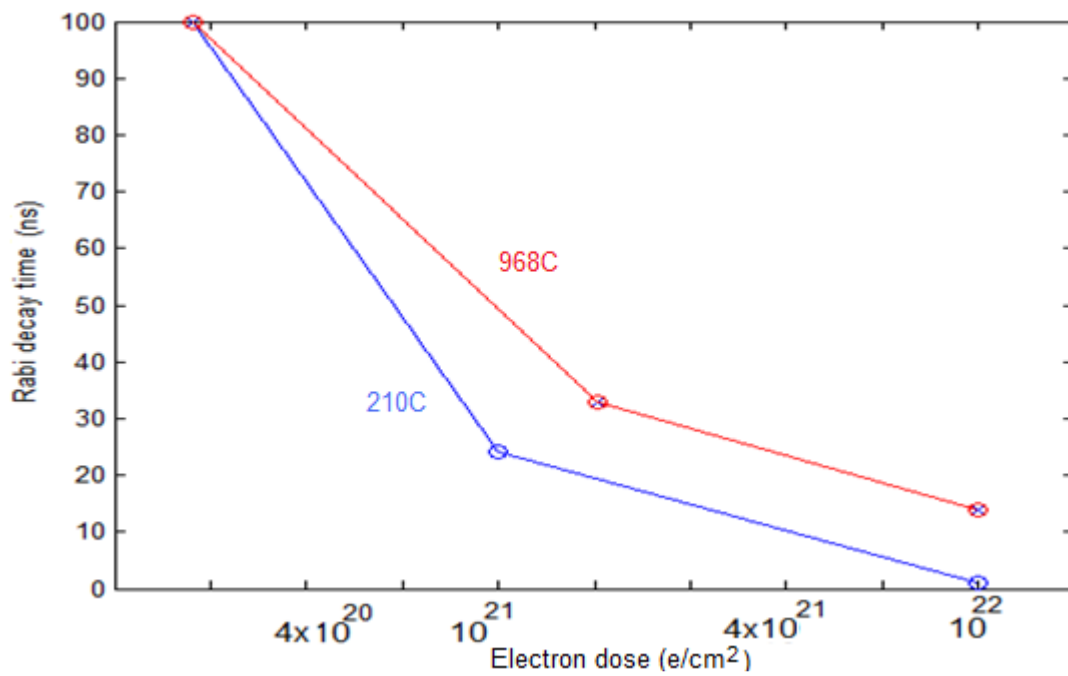Fig.4-10 Rabi decaying time with different dose.

The Rabi decaying time can be related to T2 by [31]:

$$\frac{1}{t_{Rabi,d}} = \frac{1}{2T_2} + \alpha R \; ,$$
(4.5)

where α is a constant related to noise. In reality, T2 is approximately linear to Rabi

decaying time due to small noise constant α and thus Rabi decaying time provides a way

to estimate the degree of spin relaxation as Fig. 4-10. It can be observed from the graph

that irradiation at higher temperature does increase the spin coherence.

B. Engineering nano diamond characterization

In this work, we characterize the size and effects on nitrogen-vacancy centers in NDs

by air oxidation using a combined atomic force microscopy/confocal system. The

average height reduction of individual crystals as measured by atomic force microscopy

was 10.6 nm/h at 600°C air oxidation in ambient air. The oxidation process modifies the

 surface including removal of amorphous carbon, graphite, and organic material which

leads to a decrease in background fluorescence.

The diamond nanocrystals (Microdiamant, MSY 0-0.1 µm) with a mean size of 50 nm

ranging from 0 to 100 nm as measured by an atomic force microscope (AFM), were

dispersed on a glass cover slip (Menzer-Glaser). The cover slip was laser scribed with a

5 x 5 grid consisting of $50 \times 50 \ \mu m^2$ squares (Fig. 4-11). This enabled the

identification of the same nanodiamond sites over consecutive oxidation steps.

The sample fluorescence was simultaneously measured with a confocal sample-

scanning fluorescence microscope (100× oil immersion objective lens, NA 1.4), excited
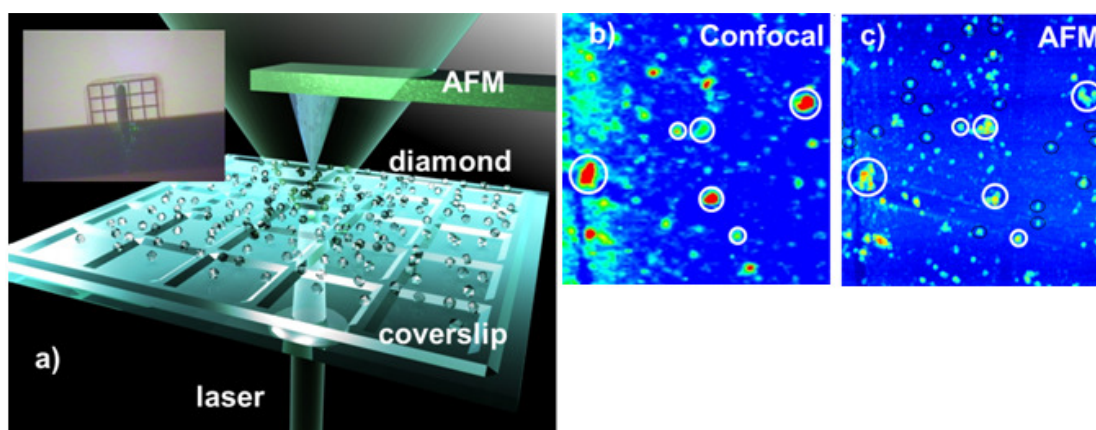
Fig. 4-11 Experimental setup. (a) shows an artistic view of the confocal beam incident from the bottom and through the glass coverslip combined with the AFM tip probing the sample from above. The inset is a photograph of the sample from directly above, one can see the laser scribed grid and the AFM cantilever. (b) is a confocal intensity map of the sample and (c) shows the corresponding AFM Height map. The scan area is 50 x 50 μm.

with a 532 nm CW diode pumped solid-state laser (Coherent, model: Compass 315-M100), and a commercial atomic force microscope (NT-MDT Ntegra) (sketch of the setup in Fig. 4-11a). Intensity autocorrelation curves were measured with a Hanbury Brown and Twiss interferometer setup consisting of 2 avalanche photodiodes (Perkin Elmer) and a correlator (Picoquant).

The oxidation process was carried out in a tube furnace (Lenton thermal designs) in air at atmospheric pressure. The sample consisted of diamond nanocrystals dispersed on a glass coverslip and placed on a metal holder inside the furnace. The furnace temperature was stabilized before the sample being inserted into the heated region. The annealing time was measured from the instant the thermocouple mounted in contact with the metal holder with the same temperature reading as the internal furnace sensor. All annealing cycles were performed at 600°C.

1. *NDs preparation*

To preparation the nanodiamonds (NDs) for optimum deaggregation before size characterization, NDs were mixed with sulphuric acid (98%, 9 ml) and nitric acid (70%, 1 ml) and then refluxed for 3 days at 70°C. The mixture was centrifuged and ultrasonicated, then refluxed again with a fresh acid mixture. The nanodiamonds were washed with distilled water then refluxed with NaOH(0.1 M, 8 ml; 1 h, 90°C), washed, then refluxed with HCl (0.1 M, 8 ml). The nanodiamond–acid mixture was washed with distilled water and ultrasonicated (1 h). The sample was diluted by addition of distilled (20 ml) and ultracentrifuged (for 1 hour with acceleration of 100,000 g). This procedure was repeated three times, and the resulting supernatant containing individual diamond grains was used for all the experiments. After preparation, the NDs were dropped on the glass cover slip mentioned above and left to dry.

2. *Photons antibunching in NDs*

The NDs were all treated with a preliminary 2 h heating step at 600°C to remove the relatively large amount of non-diamond carbon, as well as other impurities on the sample. The fact that the surface tended to have a high proportion of sp^2 was confirmed in the etch rate measurements: where an increased etch rate was measured in the early stage of annealing (see Fig. 4.13b). This can be explained by the higher etch rate of sp^2 compared to sp^3 carbon [9]. Fig. 4-12 shows the spectra for a NV centre taken before and after annealing. Before the treatment a broad unstructured fluorescence ranging from 550 nm to 800 nm was observed, which we attribute to a high graphite content at the surface of the nanodiamond (spectra is similar to [32], which is attributed

to surface defects and graphite). After 1h of heating, the spectral features originating from NV are much more pronounced. Subsequent annealing cycles do not change the spectra in a noticeable way.
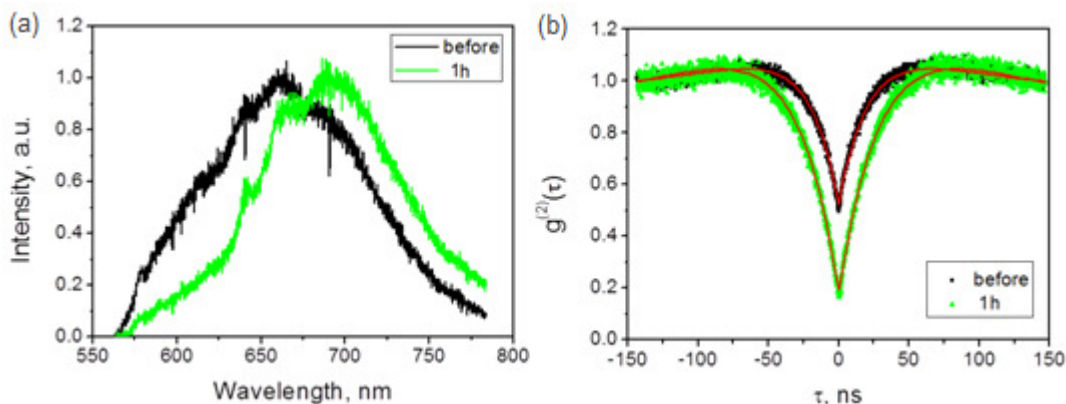
Fig. 4-12 (a) Normalised spectra of one NV site following the oxidation steps. The black line is the spectra without air oxidation, and the green one shows the spectra after 1h air oxidation. (b) shows the corresponding autocorrelation $g^2(\tau)$ curves. Note that the contrast of the antibunching feature increases.

The autocorrelation curve shows in a similar way an increase in the visibility of the antibunching dip, which means that the background fluorescence level decreased after the first air oxidation step. This also supports our assertion of the preferential removal of graphitic and other non-diamond carbon material in the early oxidation stage [9], after which the etching is almost exclusively of diamond.

3. *NDs size measurement*

A histogram of the height of individual crystals was acquired from the AFM measurements after consecutive annealing steps which gave an indication of the average change in size as a function of anneal time. The height values were obtained by fitting 2-dimensional Gaussians to individual crystals on the AFM image after subtracting the

background height offset.

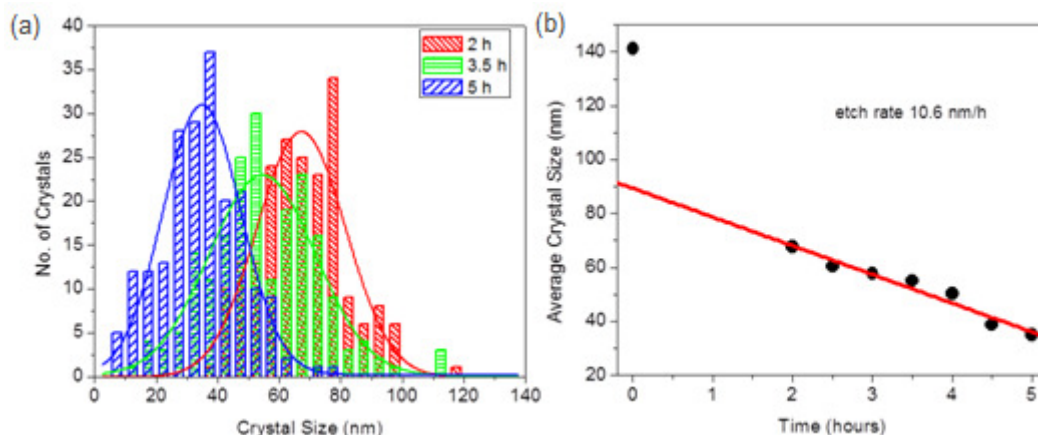Fig. 4-13 Size reduction as a function of time of nanodiamonds treated in air at 600°C. (a) Histograms of the nanodiamond sizes after a specific oxidation time. These distributions are measured consecutively on the same sample. The solid lines are Gaussian fits to the size distribution. (b) The mean of the size distributions plotted over time. A linear fit (solid line) indicates an etch rate of 10.6 nm/h.

   By fitting Gaussians to the height distributions we are able to infer a "mean" crystal size after each step. In Fig. 4-13(b) the mean sizes are plotted as a function of time and fitted with a line to give the average etch rate. Note that the first step from 0 to 2 h shows a dramatic reduction in crystal size. As discussed, this is due to the rapid etching of non-diamond carbon on the surface and this point is excluded from the linear fit made from 2 hour onward at which point the etch rate is constant. The fit indicates an etch rate of 10.6 nm/h and was determined from 7 consecutive oxidation steps, each one lasting 30 min at 600°C. Figure 4.13(a) shows the resulting histograms of nanodiamond sizes for 3 different steps within the heating cycles.

   When examining the size reduction behaviour of individual crystals, one can see that the etch rate varies somewhat. This effect is visible in Fig. 4-14 where 3 nanodiamonds

were tracked over three air oxidation steps. Two of the crystals shrink consistently in height, but one stays quite constant around 50 nm. However, the relatively crude measure of the X and Y cross sections (i.e. the width of the crystal) of this particular nanodiamond as a function of time does show a reduction. The main reason for this is an anisotropy in the etch rate for different crystallographic planes/surfaces as already observed in natural diamond [33] and CVD diamond samples [34].
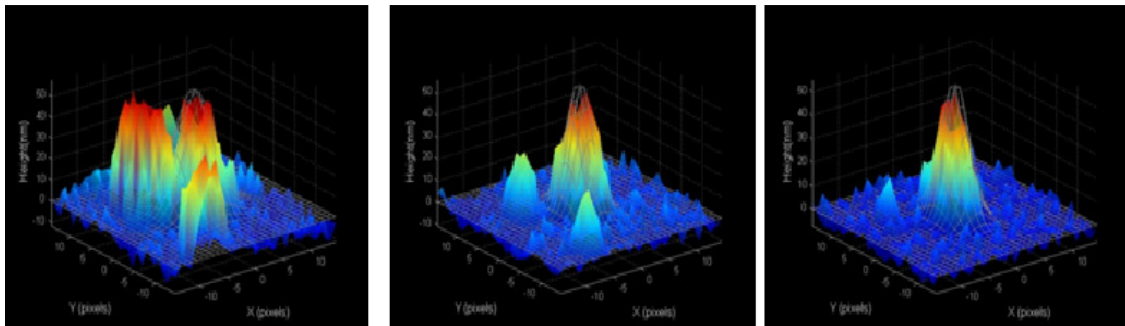
Fig. 4-14 3-dimensional AFM images of the same nanodiamonds following the oxidation steps. The crystal at the centre is not experiencing a reduction in height as much as the other 2 crystals.

More interestingly, with our experimental apparatus, we can now study the size of individual nanodiamond particles hosting NV defects. To do this, we need a confocal image of the nanodiamonds and a corresponding AFM image of the same region. In Fig. 4-15 these images were put together for the untreated sample and two oxidation steps. Not surprisingly one can observe the annihilation of NV defects via air oxidation as layers of carbon are taken away eventually exposing and removing the NV defects themselves.

Fig. 4-15 Confocal and AFM images taken after consecutive oxidation steps. (a) confocal image taken before oxidation; the numbered circles indicate some of the NV centres we selected for the analysis. (b) confocal ima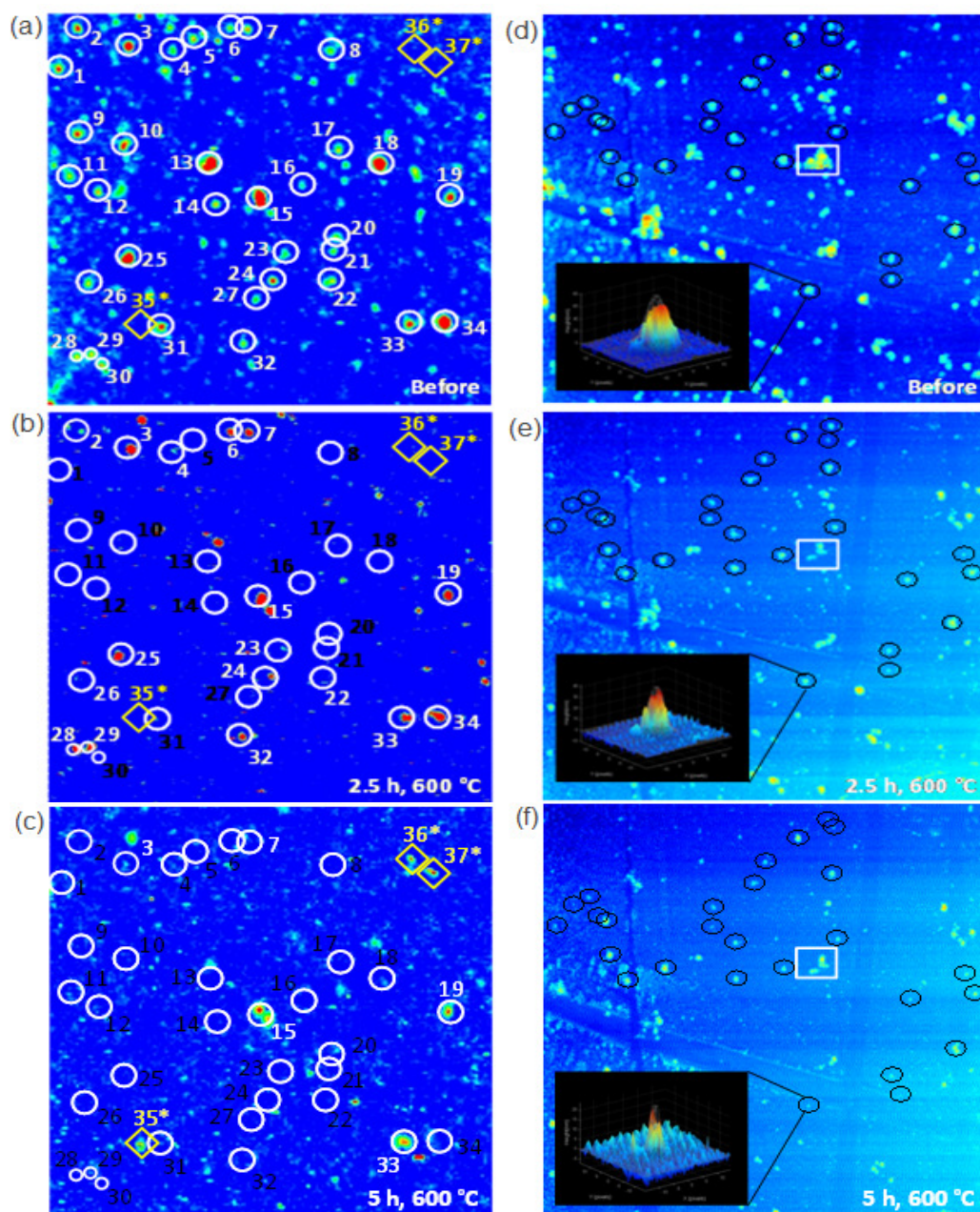ge after annealing the sample in the furnace in air for 2.5 hours at 600°C; the black-numbered circles indicate NV centres which annihilated. (c) confocal image after annealing the sample in the furnace for another 2.5 hours at 600°C. The *-numbered diamonds indicate NV centres which were created by the heating process due to vacancy diffusion to existing N_s sites. (d) AFM image taken before oxidation; the circles indicate some of the crystal we selected for the analysis. (e) AFM image after annealing the sample in the furnace for 2.5 hours at 600°C. (f) AFM image after annealing the sample in the furnace for another 2.5 hours at 600°C. The insets show the reduction in size for the highlighted crystal. The square box shows an example of diamond crystals from being clustered together to being isolated.

With these results we can determine the size distribution of the nanodiamonds hosting NV centers (see Fig. 4-16). Even though the size distribution of the powder used is specified to be ranging from 0 to 100 nm we can find particles up to 170 nm in height. This may be due to aggregation of the nanodiamonds. The air oxidation and the resulting shrinking of the nanodiamonds help to get rid of the aggregates, as shown in Fig. 4-13 the smallest nanodiamond that we observed in this study which still hosted an NV was 8 nm in height. To increase the probability of ending up with even smaller nanodiamonds containing NVs, one needs to increase the starting concentration of available NVs, which can be done by implanting the diamond powder with electrons or ions [16].
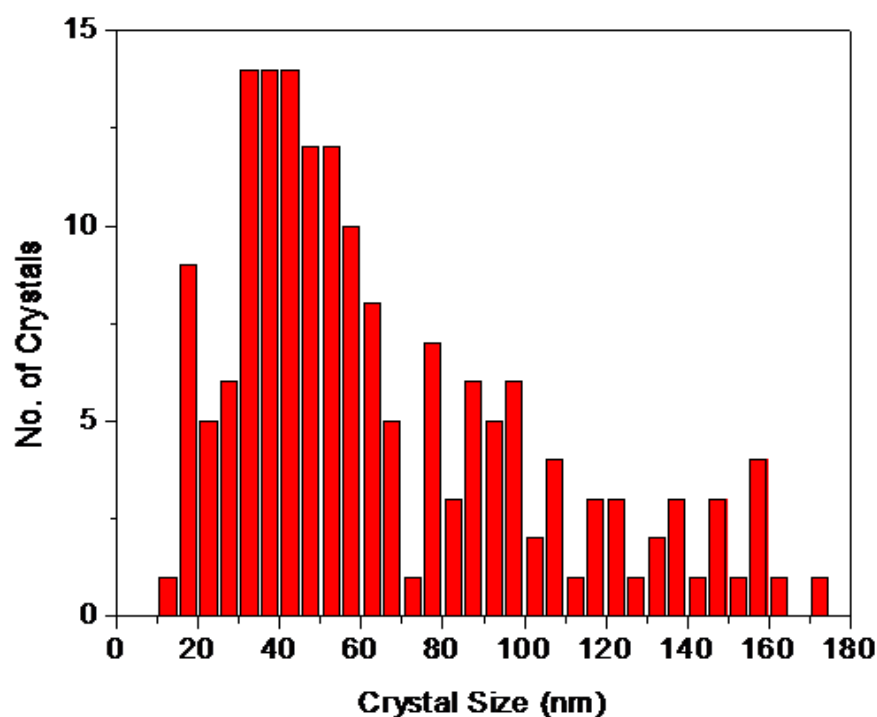

Fig. 4-16 Size distribution of the nanodiamonds hosting NV centres.

CHAPTER V

CONCLUSION AND OUTLOOK

The maximum production yield the NV centers in bulk diamond are found by both experimental and simulation: implantation at a dose of 10 N/nm^2 and annealing temperature beyond 850°C. For best magnetic sensitivity, the optimum dose of implantation is found to be 0.4 N/nm^2 with optimum temperature beyond 1000°C. It can also be concluded that hot irradiation/implantation at 1000°C will lead to better magnetic sensitivity than room temperature irradiation/implantation followed by 1000°C annealing. In addition, the enhancement of optical performance and size characterization of NV centers in nanocrystals via air oxidation at 600°C are demonstrated. In summary, the recipe for optimum yield of NV centers in bulk diamonds as well as NDs is developed and discussed.

For future outlook, the NV centers can be produced efficiently with maximum performance with this recipe for magnetic sensing and magnetic imaging. Hopefully, the first magnetic sensor capable of detection of neuron activity made of NV centers in diamond can be achieved within years.

REFERENCES

[1] R. McDermott, S. Lee, B. Haken, A. H. Trabesinger, A. Pines, and J. Clarke, Proc. Nat. Acad. Sci. U.S.A. **101**, 7857 (2004)

[2] A. M. Chang, H. D. Hallen, L. Harriott, H. F. Hess, H. L. Kao, J. Kwo, R. E. Miller, R. Wolfe, J. van der Ziel, and T. Y. Chang, Appl. Phys. Lett. **61**, 1974 (1992)

[3] D. Rugar, R. Budakian, H. J. Mamin, and B.W. Chui, Nature **430**, 329 (2004).

[4] A. Gruber, A. Drabenstedt, C. Tietz, L. Fleury, J. Wratchtrup, and C. von Borczyskowski, Science **276**, 2012 (1997)

[5] G. Balasubramanian, P. Neumann, D. Twitchen, M. Markham, R. Kolesov, N. Mizuochi, J. Isoya, J. Achard, J. Beck, J. Tissler, V. Jacques, P. R. Hemmer, F. Jelezko, and J. Wratchtrup, Nature Materials **8**, 383 (2009)

[6] G. Davies and M.F. Hamer, Proc. R. Soc London. A **348**, 285 (1976)

[7] S. J. Yu, M. W. Kang, H. C. Chang, K. M. Chen, and Y. C. Yu, J. Am. Chem. Soc **127**, 17604 (2005)

[8] J. R. Rabeau, A Stacey, A. Rabeau, S. Prawer, F. Jelezko, I. Mirza, and J. Wratchtrup, Nano Lett. **7**, 3433 (2007)

[9] S. Osswald, G. Yushin, V. Mochalin, S. O. Kucheyev, and Y. Gogotsi, J. Am. Chem. Soc **128**, 11635 (2006)

[10] V. Pichot, M. Comet, M. Fousson, C. Baras, A. Senger, F. Le Normand, and D. Spitzer, Diam. Relat. Mater. **17**, 13 (2008)

[11] International Diamond Laboratories. hpht- high pressure high temperature. Retrieved 2009, from http://www.diamondlab.org/80-hpht_synthesis.htm

[12] S. Yugo, T. Kanai, T. Kimura, and T. Muto, Appl. Phys. Lett. **58**, 1036 (1991)

[13] K. Iakoubovskii, M. V. Baidakova, B. H. Wouters, A. Stesmans, G. J. Adriaenssens, A. Ya. Vul' and P. J. Grobet, Diam. Relat. Mater. **9**, 861 (2000)

[14] T. Gaebel, M. Domhan, C. Wittmann, I. Popa, F. Jelezko, J. Rabeau, A. Greentree, S. Prawer, E. Trajkov, P. R. Hemmer and J. Wratchtrup, Appl. Phys. B **82**, 243 (2006)

[15] F. Jelezko and J. Wrachtrup, J. Physics.: Condens. Matter **18**, 807 (2006).

[16] J. R. Rabeau, P. Reichart, G. Tamanyan, D. N. Jamieson, S. Prawer, F. Jelezko, T. Gaebel, I. Popa, M. Domhan, and J. Wrachtrup, Appl. Phys. Lett. **88**, 023113 (2006)

[17] P. Meystre and M. Sargent III, *Elements of Quantum Optics*, 4th ed (Springer, 2007).

[18] J. Koike, D. M. Parkin, and T. E. Mitchell, Appl. Phys. Lett. **60,** 12 (1992)

[19] X. J. Hu, Y. B. Dai, R. B. Li, H. S. Shen, and X. C. He, Solid State Commun. **122,** 45 (2002)

[20] A. Mainwood, Phys. Rev. B **49**, 7934 (1994)

[21] C. Uzan-Saguy, C. Cytermann, R. Brener, V. Richter, M. Shaanan, and R. Kalish Appl. Phys. Lett. **67**, 1194 (1995)

[22] R.C. Burns, Vesna Cvetkovic, C. N. Dodge, D. J. F. Evans, Marie-Line T Rooney, P. M. Spear, and C. M. Welbourn, J. Cryst. Growth **104**, 257 (1990)

[23] V.M. Acosta, E. Bauch, M. P. Ledbetter, C. Santori, K.-M. C. Fu, P. E. Barclay, R. G. Beausoleil, H. Linget, J. F. Roch, F. Treussart, S. Chemerisov, W. Gawlik, and D. Budker, Phys. Rev. B **80**, 115202 (2009)

[24] K. Iakoubovskii, S. Dannefaer, and A. Stesmans, Phys. Rev. B **71**, 233201 (2005)

[25] G. Davies, S. C. Lawson, A. T. Colins, A. Mainwood, and S. J. Sharp, Phys. Rev. B **46**, 13157 (1992)

[26] G. Davies, Physica B **273/274**, 15 (1999)

[27] K. Iakoubovskii, I. Kiflawi, K. Johnston, A. Collins, G. Davies, and A. Stesmans, Physica B **340/342**, 67 (2003)

[28] J. Kiprono (2008). Unpublished doctoral dissertation, University of Witwatersrand, Johannesburg, Gauteng, South Africa

[29] A.T. Collins, New Diamond Front. Carbon Technol. **17**, 47 (2007)

[30] J.M. Baker, Diam. Relat. Mater. **16**, 216 219 (2007)

[31] R. N. Shakhmuratov, F. M. Gelardi, and M. Cannas, Phys. Rev. Lett. **79**, 2963 (1997)

[32] B. R. Smith, D. W. Inglis, B. Sandnes, J. R. Rabeau, A. V. Zvyagin, D. Gruber, C. J. Noble, R. Vogel, E. Osawa, and T. Plakhotnik, Small **5,** 1649 (2009)

[33] C. J. Chu, C. Pan, J. L. Margrave, and R. H. Hauge, Diam. Relat. Mater. **4**, 1317 (1995)

[34] M. Wolfer, J. Biener, B. S. El-dasher, M. M. Biener, A. V. Hamza, A. Kriele, and C. Wild, Diam. Relat. Mater. **18**, 713 (2009)

VITA

Name: Jeson Chen

Address: Department of Electrical and Computer
Engineering, Texas A&M University, 3128 TAMU, College Station, TX 77843-3128
e-mail: jeson-chen@tamu.edu

Education

2002 Sep-2006 May
National Taiwan University, Taipei, Taiwan
Bachelor in Physics

Higher Education

2008 Sep~2011 Aug
Texas AM University, Texas, USA
M.S. in Physics

Employment

2008 Feb- May
Low Temperature Physics Laboratory, National Sun Yat-sen University, Kaohsiung, Taiwan
Research Assistant

2008 Sep- 2009 May
Physics Dept, Texas AM University, Texas, USA
Teaching Assistant

2009 Sep~present
Electrical & Computer Engineering Dept,
Texas AM University, Texas, USA
Research Assistant